

## Polarized x-rays from a magnetar

Roberto Taverna<sup>1\*</sup>, Roberto Turolla<sup>1,4</sup>, Fabio Muleri<sup>2</sup>, Jeremy Heyl<sup>3</sup>, Silvia Zane<sup>4</sup>, Luca Baldini<sup>5,6</sup>, Denis González-Caniulef<sup>3</sup>, Matteo Bachetti<sup>7</sup>, John Rankin<sup>2</sup>, Iliaria Caiazzo<sup>8</sup>, Niccolò Di Lalla<sup>9</sup>, Victor Doroshenko<sup>10</sup>, Manel Errando<sup>11</sup>, Ephraim Gau<sup>11</sup>, Demet Kırmızıbayrak<sup>3</sup>,  
5 Henric Krawczynski<sup>11</sup>, Michela Negro<sup>12,13,14</sup>, Mason Ng<sup>15</sup>, Nicola Omodei<sup>9</sup>, Andrea Possenti<sup>7</sup>, Toru Tamagawa<sup>16,17,18</sup>, Keisuke Uchiyama<sup>17,18</sup>, Martin C. Weisskopf<sup>19</sup>, Ivan Agudo<sup>20</sup>, Lucio A. Antonelli<sup>21,22</sup>, Wayne H. Baumgartner<sup>19</sup>, Ronaldo Bellazzini<sup>6</sup>, Stefano Bianchi<sup>23</sup>, Stephen D. Bongiorno<sup>19</sup>, Raffaella Bonino<sup>24,25</sup>, Alessandro Brez<sup>6</sup>, Niccolò Bucciantini<sup>26,27,28</sup>, Fiamma Capitano<sup>2</sup>, Simone Castellano<sup>6</sup>, Elisabetta Cavazzuti<sup>29</sup>, Stefano Ciprini<sup>30,22</sup>, Enrico Costa<sup>2</sup>,  
10 Alessandra De Rosa<sup>2</sup>, Ettore Del Monte<sup>2</sup>, Laura Di Gesu<sup>29</sup>, Alessandro Di Marco<sup>2</sup>, Immacolata Donnarumma<sup>29</sup>, Michal Dovčiak<sup>31</sup>, Steven R. Ehlert<sup>19</sup>, Teruaki Enoto<sup>16</sup>, Yuri Evangelista<sup>2</sup>, Sergio Fabiani<sup>2</sup>, Riccardo Ferrazzoli<sup>2</sup>, Javier A. Garcia<sup>32</sup>, Shuichi Gunji<sup>33</sup>, Kiyoshi Hayashida<sup>34†</sup>, Wataru Iwakiri<sup>35</sup>, Svetlana G. Jorstad<sup>36,37</sup>, Vladimir Karas<sup>31</sup>, Takao Kitaguchi<sup>16</sup>, Jeffery J. Kolodziejczak<sup>19</sup>, Fabio La Monaca<sup>2</sup>, Luca Latronico<sup>24</sup>, Ioannis Liodakis<sup>38</sup>, Simone Maldera<sup>24</sup>, Alberto Manfreda<sup>6</sup>, Frédéric Marin<sup>39</sup>, Andrea Marinucci<sup>29</sup>, Alan P. Marscher<sup>36</sup>, Herman L. Marshall<sup>15</sup>, Giorgio Matt<sup>23</sup>, Ikuyuki Mitsuishi<sup>40</sup>, Tsunefumi Mizuno<sup>41</sup>, Stephen C.-Y. Ng<sup>42</sup>, Stephen L. O'Dell<sup>19</sup>, Chiara Oppedisano<sup>24</sup>, Alessandro Papitto<sup>21</sup>, George G. Pavlov<sup>43</sup>, Abel L. Peirson<sup>9</sup>, Matteo Perri<sup>22,21</sup>, Melissa Pesce-Rollins<sup>6</sup>, Maura Pilia<sup>7</sup>, Juri Poutanen<sup>44,45</sup>, Simonetta Puccetti<sup>22</sup>, Brian D. Ramsey<sup>19</sup>, Ajay Ratheesh<sup>2</sup>, Roger W. Romani<sup>9</sup>, Carmelo Sgrò<sup>6</sup>, Patrick Slane<sup>46</sup>, Paolo Soffitta<sup>2</sup>, Gloria Spandre<sup>6</sup>, Fabrizio Tavecchio<sup>47</sup>, Yuzuru Tawara<sup>40</sup>, Allyn F. Tennant<sup>19</sup>, Nicholas E. Thomas<sup>19</sup>, Francesco Tombesi<sup>48</sup>, Alessio Trois<sup>7</sup>, Sergey S. Tsygankov<sup>44,45</sup>, Jacco Vink<sup>49</sup>, Kinwah Wu<sup>4</sup>, Fei Xie<sup>50</sup>

<sup>1</sup>Department of Physics and Astronomy, University of Padova, Padova I-35131, Italy

<sup>2</sup>Istituto di Astrofisica e Planetologia Spaziali, Istituto Nazionale di Astrofisica (INAF),  
25 Roma I-00133, Italy

<sup>3</sup>Department of Physics and Astronomy, University of British Columbia; Vancouver, BC V6T 1Z1, Canada

<sup>4</sup>Mullard Space Science Laboratory, University College London; Holmbury St Mary Dorking RH5 6NT, UK

<sup>5</sup>Dipartimento di Fisica Enrico Fermi, Università di Pisa, Pisa I-56127, Italy

<sup>6</sup>Istituto Nazionale di Fisica Nucleare (INFN) Sezione di Pisa, Pisa I-56127, Italy

<sup>7</sup>Osservatorio Astronomico di Cagliari, INAF, Selargius I-09047, Italy

<sup>8</sup>Theoretical AstroPhysics Including Relativity and Cosmology, Caltech, Pasadena CA 91125, USA

<sup>9</sup>Department of Physics and Kavli Institute for Particle Astrophysics and Cosmology, Stanford University, Stanford, CA 94305, USA

<sup>10</sup>Institut für Astronomie und Astrophysik, Universität Tübingen, Tübingen 72076, Germany

<sup>11</sup>Physics Department and McDonnell Center for the Space Sciences, Washington University, St. Louis, MO 63130, USA

<sup>12</sup>University of Maryland, Baltimore County, Baltimore, MD 21250, USA

- <sup>13</sup>NASA Goddard Space Flight Center (GSFC), Greenbelt, MD 20771, USA
- <sup>14</sup>Center for Research and Exploration in Space Science and Technology, NASA/GSFC, Greenbelt, MD 20771, USA
- 5 <sup>15</sup>Kavli Institute for Astrophysics and Space Research, Massachusetts Institute of Technology, Cambridge, MA 02139, USA
- <sup>16</sup>RIKEN Cluster for Pioneering Research, 2-1 Hirosawa, Wako, Saitama 351-0198, Japan
- <sup>17</sup>RIKEN Nishina Center, 2-1 Hirosawa, Wako, Saitama 351-0198, Japan
- <sup>18</sup>Tokyo University of Science, 1-3 Kagurazaka, Shinjuku, Tokyo 162-8601, Japan
- <sup>19</sup>NASA Marshall Space Flight Center (MSFC), Huntsville, AL 35812, USA
- 10 <sup>20</sup>Instituto de Astrofísica de Andalucía, 18008 Granada, Spain
- <sup>21</sup>Osservatorio Astronomico di Roma, INAF, Monte Porzio Catone 00040, Italy
- <sup>22</sup>Space Science Data Center (SSDC), Agenzia Spaziale Italiana (ASI), Roma 00133, Italy
- <sup>23</sup>Dipartimento di Matematica e Fisica, Università degli Studi Roma Tre, Roma 00146, Italy
- <sup>24</sup>INFN Sezione di Torino, Torino 10125, Italy
- 15 <sup>25</sup>Dipartimento di Fisica, Università degli Studi di Torino, Torino 10125, Italy
- <sup>26</sup>Osservatorio Astrofisico di Arcetri, INAF, Firenze 50125, Italy
- <sup>27</sup>Dipartimento di Fisica e Astronomia, Università degli Studi di Firenze, Sesto Fiorentino 50019, Italy.
- <sup>28</sup>INFN Sezione di Firenze, Sesto Fiorentino 50019, Italy
- 20 <sup>29</sup>ASI, Roma 00133, Italy.
- <sup>30</sup>INFN Sezione di Roma Tor Vergata, Roma 00133, Italy
- <sup>31</sup>Astronomical Institute of the Czech Academy of Sciences, 14100 Praha 4, Czech Republic
- <sup>32</sup>Caltech, Pasadena, CA 91125, USA
- <sup>33</sup>Yamagata University; 1-4-12 Kojirakawa-machi, Yamagata-shi 990-8560, Japan
- 25 <sup>34</sup>Osaka University; 1-1 Yamadaoka, Suita, Osaka 565-0871, Japan
- <sup>35</sup>Department of Physics, Chuo University, 1-13-27 Kasuga, Bunkyo-ku, Tokyo 112-8551, Japan
- <sup>36</sup>Institute for Astrophysical Research, Boston University, Boston, MA 02215, USA
- <sup>37</sup>Laboratory of Observational Astrophysics, St. Petersburg University, St. Petersburg 199034, Russia
- 30 <sup>38</sup>Finnish Centre for Astronomy with the European Southern Observatory, University of Turku, 20014 Turku, Finland
- <sup>39</sup>Observatoire Astronomique de Strasbourg, Université de Strasbourg, 67000 Strasbourg, France
- 35 <sup>40</sup>Graduate School of Science, Division of Particle and Astrophysical Science, Nagoya University, Furo-cho, Chikusa-ku, Nagoya, Aichi 464-8602, Japan

<sup>41</sup>Hiroshima Astrophysical Science Center, Hiroshima University, 1-3-1 Kagamiyama, Higashi-Hiroshima, Hiroshima 739-8526, Japan

<sup>42</sup>Department of Physics, The University of Hong Kong, Pokfulam, Hong Kong

<sup>43</sup>Department of Astronomy and Astrophysics, Pennsylvania State University, University Park, PA 16801, USA

<sup>44</sup>Department of Physics and Astronomy, University of Turku, 20014 Turku, Finland

<sup>45</sup>Space Research Institute of the Russian Academy of Sciences, Moscow 117997, Russia

<sup>46</sup>Center for Astrophysics, Harvard & Smithsonian, Cambridge, MA 02138, USA

<sup>47</sup>Osservatorio Astronomico di Brera, INAF, Merate 23807, Italy

<sup>48</sup>Dipartimento di Fisica, Università degli Studi di Roma Tor Vergata, Roma 00133, Italy

<sup>49</sup>Anton Pannekoek Institute for Astronomy, University of Amsterdam, 1098 XH Amsterdam, The Netherlands

<sup>50</sup>Guangxi Key Laboratory for Relativistic Astrophysics, School of Physical Science and Technology, Guangxi University, Nanning 530004, China

\*Corresponding author. E-mail: [taverna@pd.infn.it](mailto:taverna@pd.infn.it).

†Deceased

**Magnetars are neutron stars with ultra-strong magnetic fields, which can be observed in x-rays. Polarization measurements could provide information on their magnetic fields and surface properties. We observe polarized x-rays from the magnetar 4U 0142+61 using the Imaging X-ray Polarimetry Explorer, finding a linear polarization degree of  $13.5 \pm 0.8\%$  averaged over the 2–8 keV band. The polarization changes with energy: the degree is  $15.0 \pm 1.0\%$  at 2–4 keV, drops below the instrumental sensitivity around 4–5 keV, and rises to  $35.2 \pm 7.1\%$  at 5.5–8 keV. The polarization angle also changes by  $90^\circ$  around 4–5 keV. These results are consistent with a model in which thermal radiation from the magnetar surface is reprocessed by scattering off charged particles in the magnetosphere.**

Isolated neutron stars (NSs) with extremely strong magnetic fields are referred to as magnetars (1). There are about 30 confirmed magnetars known (2), many of which are detectable only during periods of enhanced activity. Magnetar emission is powered by the magnetic field, producing bursts of hard ( $\approx 10 - 100$  keV) x-rays, with luminosity  $L \approx 10^{38} - 10^{47}$  erg s<sup>-1</sup> and duration  $\approx 0.1 - 100$  s. Magnetars also exhibit persistent x-ray emission at  $L \approx 10^{33} - 10^{35}$  erg s<sup>-1</sup>, which is pulsed at spin frequencies  $f \approx 0.1 - 10$  Hz with spin-down rates,  $\dot{f} \approx -(10^{-16} - 10^{-8})$  Hz s<sup>-1</sup>. These properties indicate high magnetic fields  $B \lesssim 10^{15}$  G, assuming a standard spin-down model (3). The 0.5 – 10 keV spectrum of magnetars consists of a blackbody (BB) component (with  $kT \sim 0.1 - 1$  keV, where  $T$  is the temperature and  $k$  is the Boltzmann constant) and a power-law (PL) component with photon index  $\Gamma \sim 2 - 4$ ; the PL dominates above  $\sim 4 - 5$  keV (2, 3). Some sources exhibit a second BB component instead of the PL. Many magnetars are detected in x-rays up to  $\approx 200$  keV, where the spectrum is also dominated by the PL component.

The magnetic field surrounding magnetars is expected to differ from a pure dipole, with a non-negligible toroidal component which twists the field lines. Because charged particles flow along

closed magnetic field lines, as required to sustain the field, the region threaded by the magnetic field (the magnetosphere) becomes optically thick to Compton scattering at the cyclotron resonance frequency [resonant Compton scattering, RCS, (4)]. The BB spectral component is expected to be emitted by (multiple regions on) the cooling surface of the NS, while the PL originates from the reprocessing of thermal photons via resonant up-scattering in the magnetosphere (3).

Magnetar x-ray persistent emission is expected to be linearly polarized in two orthogonal modes, referred to as ordinary (O) and extraordinary (X), with the polarization vector either parallel or perpendicular to the plane formed by the photon propagation direction and the (local) magnetic field (5). The expected polarization degree of the emitted radiation strongly depends on the physical state of NS external layers. If radiation comes from the bare, condensed surface, the polarization is expected to be  $\lesssim 10\%$ , but a magnetized atmosphere can produce polarization  $\lesssim 80\%$  (6–8). The polarization of outgoing photons is then modified by RCS, leading to a polarization degree  $\lesssim 30\%$  in the X-mode for the PL component, independent of the initial polarization state of the thermal photons (7–9).

Because NSs cannot be spatially resolved by observations, the contributions from regions with different magnetic field orientations (and therefore with different emitted polarization orientations) are blended together, which reduces the observed polarization (10, 11). However, if the magnetic field is strong enough (5), it forces the photon polarization vectors to follow the magnetic field direction, resulting in an observed polarization almost unchanged from that at the emission (10, 11).

The magnetar 4U 0142+61 (coordinates right ascension  $01^{\text{h}} 46^{\text{m}} 22^{\text{s}}.41$ , declination  $61^{\circ} 45' 03''.2$ , J2000 equinox) has a persistent (lightly variable) x-ray flux of  $\sim 6 \times 10^{-11} \text{ erg s}^{-1} \text{ cm}^{-2}$  in the 2–10 keV range, spin frequency  $f = 0.12 \text{ Hz}$  and frequency derivative  $\dot{f} = -2.6 \times 10^{-14} \text{ Hz s}^{-1}$ ; implying a spin-down (equatorial) magnetic field of  $B \sim 1.3 \times 10^{14} \text{ G}$  (2, 12). It is visible at infrared and optical wavelengths (13), but no (pulsed) radio emission has been detected.

We observed 4U 0142+61 with the Imaging X-ray Polarimetry Explorer [IXPE, (14)], between 2022 January 31 and 2022 February 27, for a total on-source time of 840 ks. IXPE provides imaging polarimetry over a nominal energy band of 2–8 keV. The data were extracted and processed according to standard procedures (15). Pulsations were detected (Figure S3) at  $f = 0.115079336 \pm 6 \times 10^{-9} \text{ Hz}$  with  $\dot{f} = -(2.1 \pm 0.7) \times 10^{-14} \text{ Hz s}^{-1}$  (at MJD 59624.050547, where MJD is the modified Julian date); uncertainties are 68.3% confidence. These values are consistent with previous measurements, within the uncertainties (12). We performed a spectral analysis using the software package XSPEC (16), version 12.12.1. The data are not consistent with a single-component model, so we considered several two-component models (15). In all models we fixed the value of the foreground interstellar column density to  $0.57 \times 10^{22} \text{ cm}^{-2}$  (17); it cannot be constrained by the IXPE data due to insufficient sensitivity below 2 keV. Our best-fitting parameters for a BB+PL model (Table S2) are consistent with previous measurements (17, 18).

Polarization was measured by extracting the (calibrated) Stokes parameters  $I$ ,  $Q$  and  $U$  from each photon, collected by the three independent IXPE detector units (DUs). After subtracting the sky background, the contributions of each DU were combined, accounting for the  $120^{\circ}$  offset between the DUs. Figure 1 shows the phase-averaged, normalized Stokes parameters ( $Q/I$  and  $U/I$ ) in the 2–8 keV energy range, for the individual DUs and the combined data. The phase-

averaged, energy-integrated values are  $Q/I = 0.013 \pm 0.008$  and  $U/I = 0.120 \pm 0.008$ , implying a polarization degree,  $PD \equiv \sqrt{Q^2 + U^2}/I$ , of  $13.5 \pm 0.8\%$  and a polarization angle,  $PA \equiv \arctan(U/Q)/2$ , of  $+48.5^\circ \pm 1.6^\circ$ , with positive values being East of (local celestial) North; uncertainties are  $1\sigma$ . We derived these values using two different methods, finding consistent results (15). We determined that the minimum detectable polarization at 99% confidence level ( $MDP_{99}$ ) for our observation is  $\sim 2\%$  over the 2–8 keV range, so the significance of the non-zero polarization degree is  $\sim 17\sigma$ .

To investigate whether the PD and PA depend on the photon energy, the data were grouped into five energy bins, selected to contain similar numbers of counts in each bin. Figure 2 shows a polar plot of the results. We find the PD is  $15.0 \pm 1.0\%$  at low energies ( $\sim 2\text{--}4$  keV),  $\sim 10\sigma$  above the  $MDP_{99}$  of that bin, which is  $\sim 4\%$ . At 4–5 keV the PD is consistent with zero. In the highest energy bin (5.5–8 keV), the PD is  $35.2 \pm 7.1\%$ , where the  $MDP_{99}$  is  $\sim 21\%$ . The PA is about  $50^\circ$  at energies below 4 keV and  $-40^\circ$  above 5 keV, a swing of  $90^\circ$ .

We also performed a spectro-polarimetric analysis, by separately convolving the low- and high-energy spectral components with a constant polarization model (POLCONST in XSPEC). This confirms the  $90^\circ$  swing in polarization angle for all the two-component spectral models we considered: BB+BB, BB+PL and BB+Truncated PL (15). For the latter model, the derived PD for the two components is within  $\sim 1\sigma$  of the observed values, with the low energy BB component being less polarized than the high-energy PL (15).

To perform a phase-dependent analysis, we divided the flux into 100 phase bins and used an unbinned maximum likelihood technique (19) to determine the PD and PA. Figure 3A shows the resulting pulse profile, which is double-peaked, as found in previous observations (18). Phase variations are evident in both PD and in PA (Fig. 3B–C), with amplitudes of  $\sim 10\%$  and  $\sim 30^\circ$ , respectively. At low energies (2–4 keV), we find the main and secondary peaks have higher polarization fraction ( $\sim 15\%$ ) than the phase valley between them ( $\sim 9\%$ ). In contrast, the phase-resolved PA is single peaked. This is consistent with the predictions of pulsar (a different type of NS) models [specifically the rotating-vector model (20)], although a strong degeneracy prevents us from determining the NS spin and magnetic axes orientations from the PA data (15).

A phase-resolved spectral analysis of 4U 0142+61 shows no statistically significant dependence of the spectrum on rotational phase (15). The blackbody component is compatible with being constant in phase (Fig. S5), consistent with previous results (21) and previous observations of a low pulsed fraction ( $\sim 5\%$ ) below 3–4 keV (18).

We considered the IXPE results within a twisted-magnetosphere model (4), accounting for the quantum electrodynamical effect of vacuum birefringence (7–9). The observed polarization behavior as a function of energy – with a minimum PD and a  $90^\circ$  swing of PA at 4–5 keV – indicates that the 2–8 keV x-ray emission from 4U 0142+61 has two distinct components, polarized in two different normal modes, which correspond to the two components identified in the spectral analysis. In this framework, the low-energy component is produced by thermal emission from the surface of the NS, while the high-energy component is produced by photons scattered to higher energies in the magnetosphere (Figure 4A). The measured polarization fraction at high energies ( $\sim 35\%$  at 5.5–8 keV) is compatible with the theoretical prediction of the RCS model (7) and indicates that X-mode photons dominate at high energies; conversely, O-mode photons dominate at low energies.

Theoretical models for magnetar surface emission of soft x-rays predict either i) a large ( $\gtrsim 50\%$ ) polarization degree in the X-mode, if there is a gaseous atmosphere heated from below (22); or ii) a small  $\lesssim 10\%$  polarization degree in the O-mode, if there is a condensed (solid/liquid) surface (6–8, 23). The IXPE result below 4 keV is not compatible with the presence of an atmosphere and only marginally compatible with a condensed surface. The latter would be more consistent with the data if the PD could be raised in the model, perhaps by thermal radiation being emitted from only a limited region, not the entire surface (as was assumed in previous calculations). The low pulsed fraction at low energies (18) indicates an extended emitting area. Using a numerical code (7), we calculated that radiation from a condensed iron surface, emitted from an equatorial belt, produces O-mode photons at low energies (2–4 keV) with PD  $\sim 15\%$ . Reprocessing by RCS then produces an excess of X-mode photons at higher energies (5.5–8 keV) with PD  $\sim 35\%$ , while the PA changes by  $90^\circ$ . Our calculation does not assume that the reference direction in the plane of the sky (from which the PA is computed) coincides with the projection of the NS spin axis. To match the measured and predicted (absolute) values, an offset is added to the simulated PA (15). Figure 2 shows the results of our numerical simulation for a magnetic field strength  $\sim 10^{14}$  G, as measured for 4U 0142+61 (18), assuming the emissivity of an iron condensed surface (23), in the fixed-ion approximation. A hotter belt close to the magnetic equator appears in NS magneto-thermal evolution calculations, in both two and three dimensions (24, 25).

We also consider alternative models to explain the IXPE data. Within the RCS paradigm, low-energy O-mode photons could be produced by a gaseous layer with an inverted temperature profile, with a downward flow of energy, as might be produced by external particle bombardment (26). In this case, O-mode photons would escape from a deeper (and so hotter) region than in a passively cooling atmosphere, and would dominate the outgoing flux.

In an alternative scenario, the low-energy emission could be interpreted as polarized in the X-mode and the high energy emission, above 4–5 keV, in the O-mode. Low-energy, X-mode dominated emission with a low polarization degree ( $\sim 15\%$ ) could originate from an extended region of a condensed iron surface seen few degrees away from the magnetic axis. Radiation from a thin atmosphere or corona, in the presence of thermal photons undergoing Compton scattering (8) could produce the observed polarization at low energies. However, this scenario does not explain how O-mode photons would dominate the emission in the 5–8 keV band. Saturated Compton scattering in a thin atmosphere or corona (8) or emission from an electron-positron plasma (27) could potentially produce O-mode dominated radiation (Figure 4B), but these models predict a much higher PD than is observed. Emission from a small region of the surface that is covered by an externally illuminated gaseous layer but hot enough to dominate the high-energy band, would also produce substantial polarization in the O-mode. No detailed modeling of these scenarios is available.

Identifying the mode in which the observed x-ray photons are predominantly polarized would determine the orientation of the magnetar spin axis projected onto the plane of the sky. The phase-averaged PA is  $0^\circ$  (or  $90^\circ$ ) for radiation mostly polarized in the O-mode (or X-mode), taking the reference direction in the plane of the sky to be along the spin axis projection (10). If O-mode photons dominate at low energies where  $PA \sim 50^\circ$ , as in the RCS model, the projection of the spin axis would be  $\sim 50^\circ$  East of North. Conversely, if low-energy photons are polarized in the X-mode the spin axis projection would be  $\sim 40^\circ$  West of North. In the latter case, the spin projection would be consistent with the direction of the magnetar proper motion,  $60^\circ \pm 12^\circ$  West of North (28) (Figure 2), while in the former case the two would be almost orthogonal. It is

unclear which is more appropriate for magnetars. Observations of pulsars (including the Crab Pulsar and Vela Pulsar) show alignment of the spin axis with the proper motion (29). On the other hand, binary star evolution theory predicts that NSs should be accelerated perpendicular to their spin axis during their formation process (30). We are unable to distinguish between these possibilities.

5

We have detected (linearly) polarized x-ray emission from the magnetar 4U 0142+61. The polarization properties vary with x-ray energy, including a 90° swing of the polarization angle. These observations can be explained by a model of emission from the bare condensed surface of the NS, reprocessed by RCS in a twisted magnetosphere. Alternative explanations are also possible.

10

## References and Notes

1. R. C. Duncan, C. Thompson, Formation of very strongly magnetized neutron stars: Implication for gamma-ray bursts. *Astrophys. J. Lett.* **392**, L9 (1992).
2. S. A. Olausen, V. M. Kaspi, The McGill Magnetar Catalog. *Astrophys. J., Suppl. Ser.* **212**, 6 (2014).
3. V. M. Kaspi, A. M. Beloborodov, Magnetars. *Annu. Rev. Astron. Astrophys.* **55**, 261 (2017).
4. C. Thompson, M. Lyutikov, S. R. Kulkarni, Electrodynamics of magnetars: Implications for the persistent x-ray emission and spin-down of the soft gamma repeaters and anomalous x-ray pulsars. *Astrophys. J.* **574**, 332 (2002).
5. A. K. Harding, D. Lai, Physics of strongly magnetized neutron stars. *Rep. Prog. Phys.* **69**, 2631 (2006).
6. D. González-Caniulef, S. Zane, R. Taverna, R. Turolla, K. Wu, Polarized thermal emission from X-ray dim isolated neutron stars: the case of RX J1856.5-3754. *Mon. Not. R. Astron. Soc.*, **459**, 3585 (2016).
7. R. Taverna, R. Turolla, V. Suleimanov, A. Y. Potekhin, S. Zane, X-ray spectra and polarization from magnetar candidates. *Mon. Not. R. Astron. Soc.* **492**, 5057 (2020).
8. I. Caiazzo, D. González-Caniulef, J. Heyl, R. Fernández, Probing magnetar emission mechanisms with X-ray spectropolarimetry. *Mon. Not. R. Astron. Soc.* **514**, 5024 (2022).
9. R. Fernández, S. W. Davis, The x-ray polarization signature of quiescent magnetars: Effect of magnetospheric scattering and vacuum polarization. *Astrophys. J.* **730**, 131 (2011).
10. R. Taverna *et al.*, Polarization of neutron star surface emission: a systematic analysis. *Mon. Not. R. Astron. Soc.* **454**, 3254 (2015).
11. J. S. Heyl, N. J. Shaviv, D. Lloyd, The high-energy polarization-limiting radius of neutron star magnetospheres – I. slowly rotating neutron stars. *Mon. Not. R. Astron. Soc.* **342**, 134 (2003).
12. R. Dib, V. M. Kaspi, 16 yr of RXTE monitoring of five anomalous x-ray pulsars. *Astrophys. J.* **784**, 37 (2014).
13. F. Hulleman, M. H. van Kerkwijk, S. R. Kulkarni, An optical counterpart to the anomalous X-ray pulsar 4U0142+61. *Nature* **408**, 689 (2000).
14. M. C. Weisskopf *et al.*, The Imaging X-ray Polarimetry Explorer: Pre-Launch. *J. Astron. Telesc. Instrum. Syst.* **8**, 026002 (2022).
15. Materials and methods are available as supplementary materials.
16. K. A. Arnaud, “XSPEC: The First Ten Years” in Astronomical Data Analysis Software and Systems V, G. H. Jacoby and J. Barnes, Eds. (Astronomical Society of the Pacific Conference Series, 1996), vol. 101, pp. 17.
17. P. R. den Hartog *et al.*, Detailed high-energy characteristics of AXP 4U 0142+61: Multi-year observations with INTEGRAL, RXTE, XMM-Newton, and ASCA. *Astron. Astrophys.* **489**, 245 (2008).
18. N. Rea *et al.*, Very deep x-ray observations of the anomalous x-ray pulsar 4U0142+614. *Mon. Not. R. Astron. Soc.* **381**, 293 (2007).

19. D. González-Caniulef, I. Caiazzo, J. Heyl, <https://arxiv.org/abs/2204.00140>.
20. V. Radhakrishnan, D. J. Cooke, Magnetic poles and polarization structure of pulsar radiation. *Astrophys. J. Lett.* **3**, 225 (1969).
21. S. P. Tendulkar *et al.*, Phase-resolved NuSTAR and Swirt-XRT observations of magnetar 4U 0142+61. *Astrophys. J.* **808**, 32 (2015).
22. A. Y. Potekhin, G. Chabrier, W. C. G. Ho, Opacities and spectra of hydrogen atmospheres of moderately magnetized neutron stars. *Astron. Astrophys.* **572**, A69 (2014).
23. A. Y. Potekhin, V. F. Suleimanov, M. van Adelsberg, K. Werner, Radiative properties of magnetic neutron stars with metallic surfaces and thin atmospheres. *Astron. Astrophys.* **546**, A121 (2012).
24. D. Viganò, “Magnetic fields in neutron stars”, thesis, Universidad de Alicante, Alicante, Spain, <https://arxiv.org/abs/1310.1243> (2013).
25. D. De Grandis *et al.*, X-ray emission from Isolated Neutron Stars revisited: 3D magnetothermal simulations. *Astrophys. J.* **914**, 118 (2021).
26. D. González-Caniulef, S. Zane, R. Turolla, K. Wu, Atmosphere of strongly magnetized neutron stars heated by particle bombardment. *Mon. Not. R. Astron. Soc.* **483**, 599 (2019).
27. C. Thompson, A. Kostenko, Pair plasma in super-QED magnetic fields and the hard x-ray/optical emission of magnetars. *Astrophys. J.* **904**, 184 (2020).
28. S. P. Tendulkar, P. B. Cameron, S. R. Kulkarni, Proper motions and origins of AXP 1E 2259+586 and AXP 4U 0142+61. *Astrophys. J.* **772**, 31 (2013).
29. H. T. Janka, A. Wongwathanarat, M. Kramer, Supernova fallback as origin of neutron star spins and spin-kick alignment. *Astrophys. J.* **926**, 9 (2022).
30. M. Colpi, I. Wasserman, Formation of an evanescent proto-neutron star binary and the origin of pulsar kicks. *Astrophys. J.* **581**, 1271 (2002).
31. P. Soffitta *et al.*, The instrument of the imaging x-ray polarimetry explorer. *Astron. J.* **162**, 208 (2021).
32. L. Baldini *et al.*, Design, construction and test of the gas pixel detectors for the IXPE mission. *Astropart. Phys.* **133**, 102628 (2021).
33. L. Baldini *et al.*, IXPEOBSSIM: A simulation and analysis framework for the imaging X-ray polarimetry explorer. *SoftwareX* **19**, 101194 (2022).
34. Retrievable at <https://heasarc.gsfc.nasa.gov/docs/ixpe/caldb>.
35. W. A. Joye, E. Mandel, “New Features of SAOImage DS9” in *Astronomical Data Analysis Software and Systems XII*, H. E. Payne, R. I. Jedrzejewski, R. N. Hook, Eds. (Astronomical Society of the Pacific Conference Series, 2003), vol. 295, pp. 489.
36. W. M. Folkner, J. G. Williams, D. H. Boggs, The Planetary and Lunar Ephemeris DE 421. *JPL Interplan. Net. Prog. Rep.* **42**, 178 (2009).
37. R. Buccheri *et al.*, Search for pulsed  $\gamma$ -ray emission from radio pulsars in the COS-B data. *Astron. Astrophys.* **128**, 245 (1983).
38. M. Bachetti, Astrophysics Source Code Library, ascl:1805.019 (2018).

39. M. Bachetti *et al.*, Extending the  $Z_n^2$  and H statistics to generic pulsed profiles. *Astrophys. J.* **909**, 33 (2021).
40. D. Huppenkothen *et al.*, Stingray: A modern python library for spectral timing. *Astrophys. J.* **881**, 39 (2019).
- 5 41. O. C. de Jager, B. C. Raubenheimer, J. W. H. Swanepoel, A powerful test for weak periodic signals with unknown light curve shape in sparse data. *Astron. Astrophys.* **221**, 180 (1989).
42. B. A. Vaughan *et al.*, Search for millisecond pulsations in low-mass x-ray binaries. II. *Astrophys. J.* **435**, 362 (1994).
43. K. T. S. Brazier, Confidence intervals from the Rayleigh test. *Mon. Not. R. Astron. Soc.* **268**, 709 (1994).
- 10 44. M. Bachetti *et al.*, Orbital Decay in M82 X-2, *Astrophys. J.* **937**, 125 (2022).
45. J. H. Taylor, Pulsar timing and relativistic gravity. *Philosophical Transactions: Physical Sciences and Engineering* **341**, 117 (1992).
46. J. Luo *et al.*, PINT: A modern software package for pulsar timing. *Astrophys. J.* **911**, 45 (2021).
- 15 47. J. Wilms, A. Allen, R. McCray, On the absorption of x-rays in the interstellar medium. *Astrophys. J.* **542**, 914 (2000).
48. M. Durant, M. H. van Kerkwijk, Multiwavelength variability of the magnetar 4U 0142+61. *Astrophys. J.* **652**, 576 (2006).
- 20 49. M. Tsujimoto *et al.*, Cross-calibration of the X-ray instruments onboard the Chandra INTEGRAL, RXTE, Suzaku, Swift, and XMM-Newton observatories using G21.5-0.9, *Astron. Astrophys.*, **525**, A25 (2011).
50. F. Kislat, B. Clark, M. Beilicke, H. Krawczynski, Analyzing the data from x-ray polarimeters with Stokes parameters. *Astropart. Phys.* **68**, 45 (2015).
- 25 51. A. Di Marco *et al.*, A weighted analysis to improve the x-ray polarization sensitivity of the imaging x-ray polarimetry explorer. *Astron. J.* **163**, 170 (2022).
52. A. L. Peirson, R. W. Romani, Toward optimal signal extraction for imaging x-ray polarimetry. *Astrophys. J.* **920**, 40 (2021).
53. J. Rankin *et al.*, An algorithm to calibrate and correct the response to unpolarized radiation of the x-ray polarimeter onboard IXPE. *Astron. J.* **163**, 39 (2022).
- 30 54. T. E. Strohmayer, X-ray spectro-polarimetry with photoelectric polarimeters. *Astrophys. J.* **838**, 72 (2017).
55. M. C. Weisskopf, R. F. Elsner, S. L. O'Dell, On understanding the figures of merit for detection and measurement of x-ray polarization. Space Telescopes and Instrumentation 2010: Ultraviolet to Gamma Ray, M. Arnaud, S. S. Murray, T. Takahashi Eds. (Proceedings of the SPIE), vol. 7732, 10.1117/12.857357 (2010).
- 35 56. T. E. Strohmayer, T. R. Kallman, On the statistical analysis of x-ray polarization measurements. *Astrophys. J.* **773**, 103 (2013).
57. F. Muleri, <https://arxiv.org/abs/2204.12739> (2022).

58. J. Poutanen, Relativistic rotating vector model for x-ray millisecond pulsars. *Astron. Astrophys.* **614**, 166 (2020).

**Acknowledgments:** We thank three anonymous referees for helpful and constructive comments that improved the paper.

This paper is based on observations made by the IXPE, a joint US and Italian mission. The US contribution to the IXPE mission is supported by NASA, led and managed by the MSFC, with industry partner Ball Aerospace (contract NNM15AA18C). The Italian contribution is supported by ASI through contract ASI-OHBI-2017-12-I.0, agreements ASI-INAF-2017-12-H0 and ASI-INFN-2017.13-H0 and the SSC with agreements ASI-INAF-2022-14-HH.0 and ASI-INFN 2021-43-HH.0, and by INAF and INFN. Data products were provided by the IXPE Team (MSFC, SSC, INAF and INFN) and distributed with additional software tools by the High-Energy Astrophysics Science Archive Research Center (HEASARC) at NASA GSFC.

**Funding:** R. Ta. and R. Tu. acknowledge financial support from the Italian MUR through grant PRIN 2017LJ39LM. JH, DGC, IC and DK acknowledge the support of the Natural Sciences and Engineering Research Council of Canada (NSERC), funding reference number 5007110, and the Canadian Space Agency. DGC is a Canadian Institute for Theoretical Astrophysical (CITA) National Fellow (grant #CITA 490888-16). EG and HK acknowledge NASA support under grants 80NSSC18K0264, 80NSSC22K1291, 80NSSC21K1817 and NNX16AC24G. M. Ne. acknowledges support from NASA under award 80GSFC21M0002. TT was supported by Grant JSPS KAKENHI JP19H05609. FM, JR, SB, EC, EDM, ADM, YE, SF, RF, FLM, GM, M. Pe., AR, P. So. and AT were supported by ASI and INAF under grants ASI-INAF-2017-12-H0 and ASI-INAF-2022-14-HH.0. LB, LL, R. Be., R. Bo., AB, S. Ca., SM, A. Ma., CO, MPR, CS, GS were supported by ASI and INFN under grants ASI-INFN-2017.13-H0 and ASI-INFN-2021-43-HH.0.

**Author contributions:** R. Ta., R. Tu., FM, JH, SZ, LB, JR and MCW planned the observing campaign. R. Ta., R. Tu., FM, JH, SZ, LB, JR, DGC, MB, IC, NDL, EG, DK, HK, M. Ne., M. Ng, NO, AP, TT, KU analyzed the data. R. Ta., R. Tu., FM, JH, SZ, LB, JR, DGC, MB, IC, AP, TT, KU modeled the data. R. Ta., R. Tu., FM, JH, SZ, LB, JR, DGC, MB, AP wrote the manuscript. VD and ME served as internal reviewers. All the other authors contributed to the design and science case of the IXPE mission, and to the planning of the observations in this paper. All authors provided input and comments on the manuscript.

**Competing interests:** The authors declare there are no competing interests.

**Data and materials availability:** The IXPE observation of 4U 0142+61 is available in the High Energy Astrophysics Science Archive Research Center (HEASARC) IXPE Data Archive <https://heasarc.gsfc.nasa.gov/docs/ixpe/archive/> under ObsID 01003299. The IXPE software is available at <https://github.com/lucabaldini/ixpeobssim> and <https://ixpeobssim.readthedocs.io/en/latest/?badge=latest>. The measured polarizations are listed in Table S2 and the results of our model fitting are listed in Tables S1 and S3. The code used for producing the equatorial belt simulation reported in Fig. 2 is available at <https://github.com/robertotaverna/magMC> (DOI 10.5281/zenodo.7215778).

## Supplementary Materials

Materials and Methods

Figs. S1 to S10

Tables S1 to S3

References (31–58)

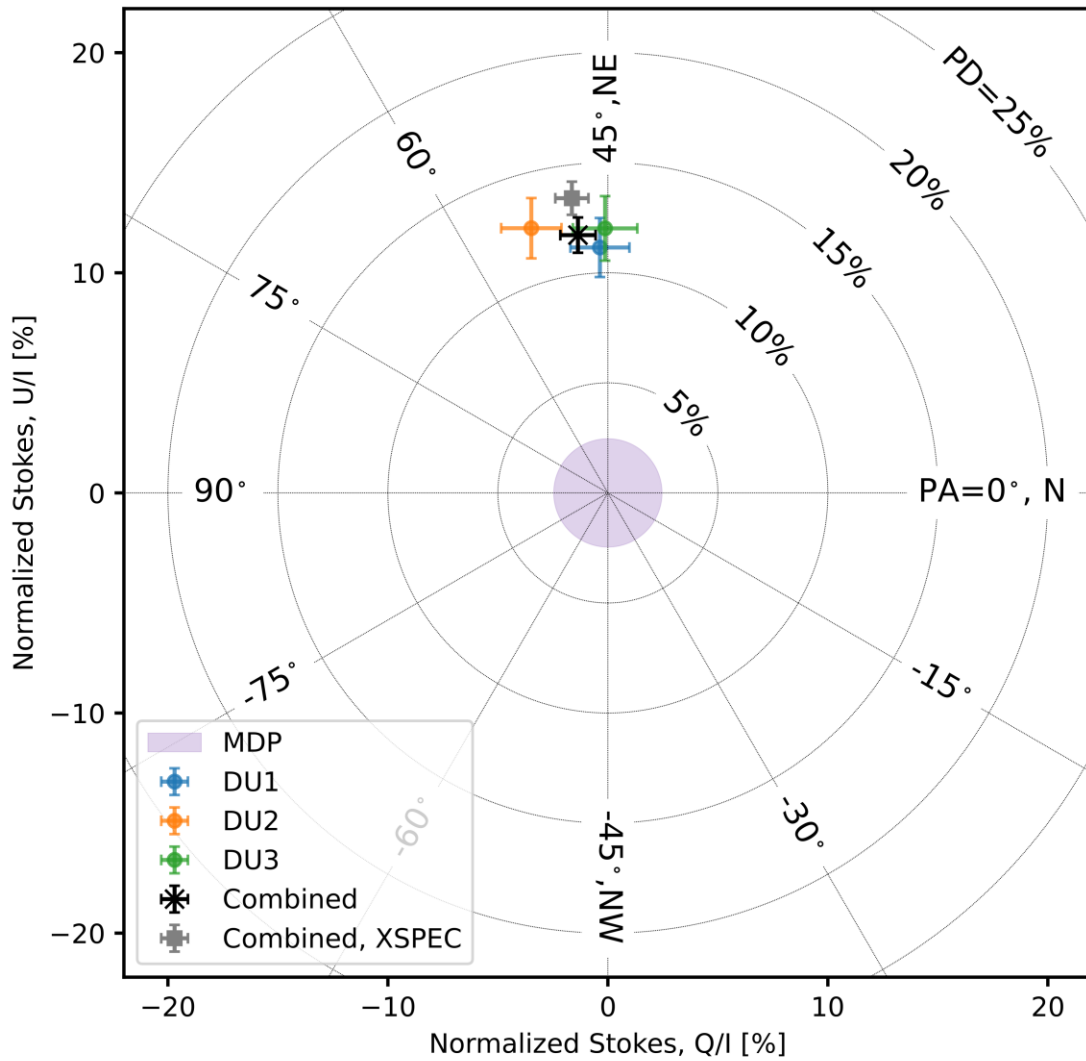


**Fig. 1. Normalized, background-subtracted Stokes parameters  $Q/I$  and  $U/I$  for x-ray emission from 4U 0142+61.**

The values measured from each of the three IXPE DUs (in the 2–8 keV range) are marked by green, orange and blue circles with  $1\sigma$  error bars, while their combinations obtained using two approaches (15) are shown by the black cross and the gray square, respectively. The background circles indicate PD and the radial lines indicate PA, measured East from North. The purple shaded area shows the detection limit ( $MDP_{99}$ ) for the combined measurement.

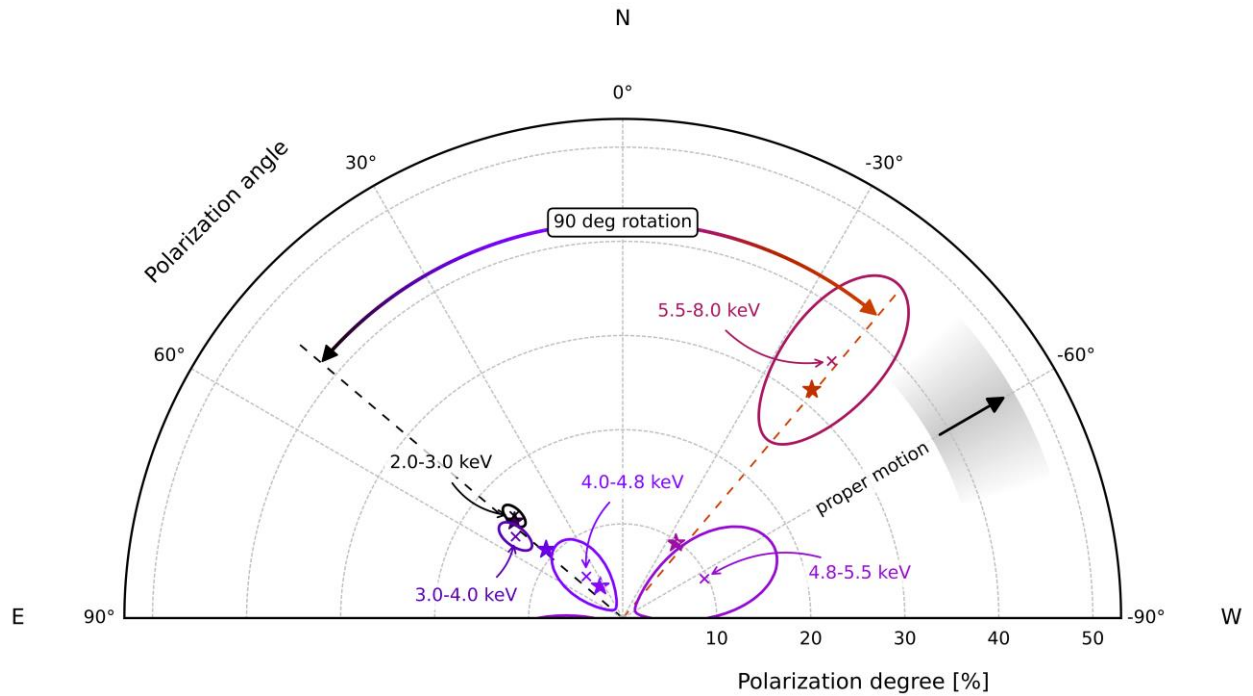


**Fig. 2. Polar plot showing the energy dependence of the measured PD and PA.**

Crosses indicate the measured values, in labelled energy bins, and contours enclose the 68.3% confidence level regions obtained with XSPEC (15). Stars indicate the corresponding PD and PA calculated using the condensed-surface RCS model. The arc bounded by the two dashed lines shows the change in polarization angle from the lowest (2–3 keV, black dashed line) to the highest (5.5–8 keV, red dashed line) energy bins. The black arrow and gray shaded area indicate the proper motion direction of the source and its associated uncertainty (28).

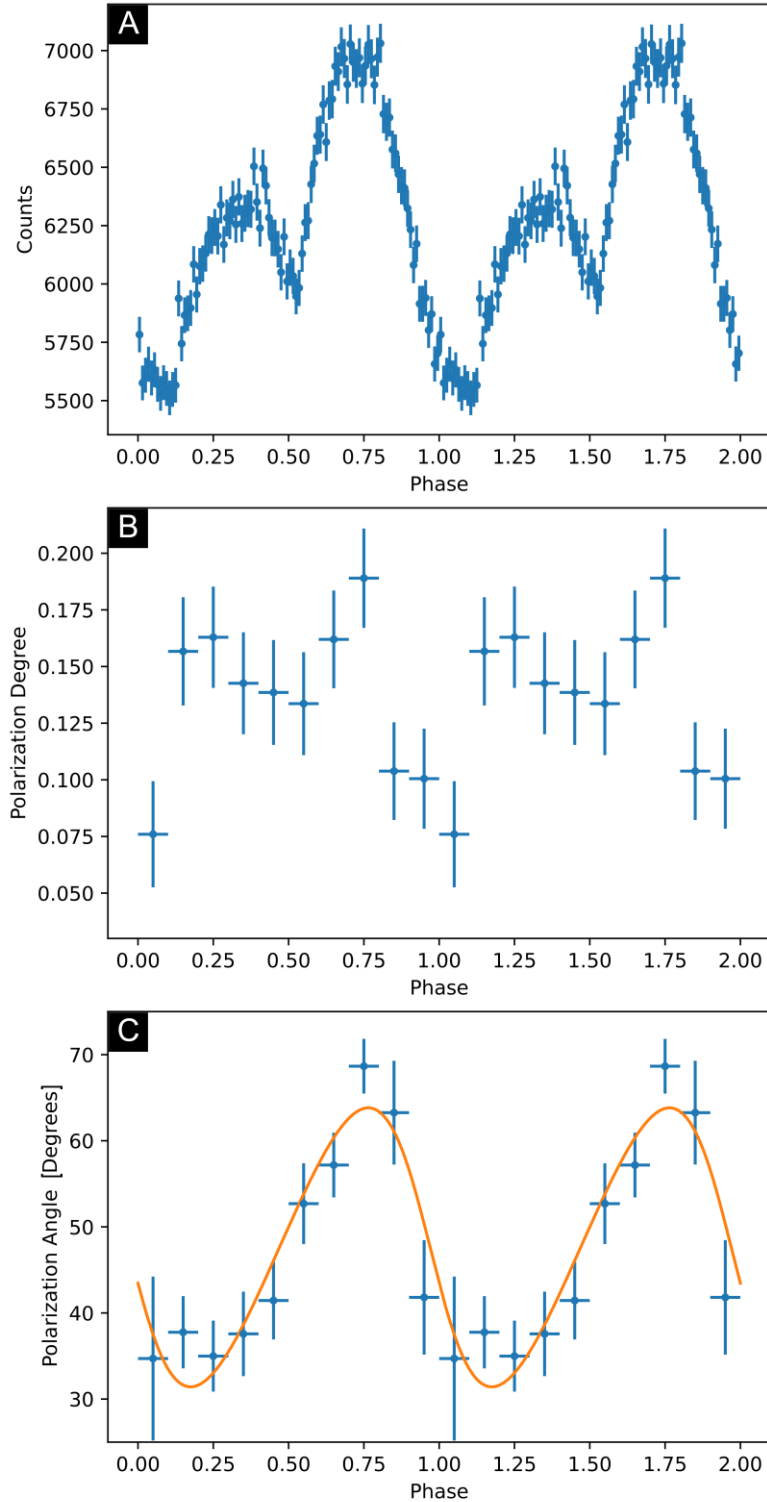


**Fig 3. Phase-dependent x-ray flux and polarization properties.**

(A) Energy-integrated (2–8 keV) IXPE counts as a function of spin phase. Error bars are at  $1\sigma$  confidence level. (B) Polarization degree as a function of spin phase. Error bars indicate  $\Delta \log L = 1$ , where  $L$  is the unbinned likelihood (19). (C) Same as panel B, but for the polarization angle. The orange curve shows the best-fitting rotating vector model (15).

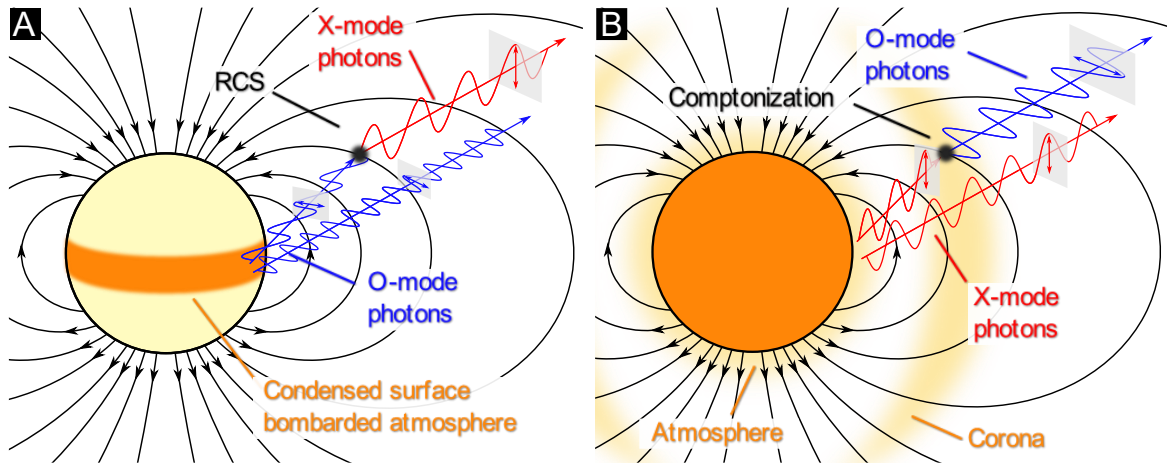


**Fig 4. Schematic illustration of the proposed theoretical scenarios.**

5 (A) Thermal radiation emitted by an equatorial belt on the condensed surface of the magnetar (or an atmosphere with an inverted temperature gradient), then reprocessed by RCS in the magnetosphere. (B) Radiation from the whole surface reprocessed by (unsaturated) thermal Compton scattering in a near-surface atmospheric layer, then additional (saturated) Compton scattering in an extended corona. The dark orange areas on the NS surface indicate the emitting regions. Black lines with arrows indicate the (dipole) magnetic field lines. The gray rectangles along the photon trajectories highlight the polarization plane and the oscillating electric field.

## Supplementary Materials for

## Polarized x-rays from a magnetar

Roberto Taverna\*, Roberto Turolla, Fabio Muleri, Jeremy Heyl, Silvia Zane, Luca Baldini,  
Denis González-Caniulef, Matteo Bachetti, John Rankin, Iaria Caiazzo, Niccolò Di Lalla, Victor  
Doroshenko, Manel Errando, Ephraim Gau, Demet Kırmızıbayrak, Henric Krawczynski,  
Michela Negro, Mason Ng, Nicola Omodei, Andrea Possenti, Toru Tamagawa, Keisuke  
Uchiyama, Martin C. Weisskopf, , Ivan Agudo, Lucio A. Antonelli, Wayne H. Baumgartner,  
Ronaldo Bellazzini, Stefano Bianchi, Stephen D. Bongiorno, Raffaella Bonino, Alessandro Brez,  
Niccolò Bucciantini, Fiamma Capitanio, Simone Castellano, Elisabetta Cavazzuti, Stefano  
Ciprini, Enrico Costa, Alessandra De Rosa, Ettore Del Monte, Laura Di Gesu, Alessandro Di  
Marco, Immacolata Donnarumma, Michal Dovčiak, Steven R. Ehlert, Teruaki Enoto, Yuri  
Evangelista, Sergio Fabiani, Riccardo Ferrazzoli, Javier A. Garcia, Shuichi Gunji, Kiyoshi  
Hayashida, Wataru Iwakiri, Svetlana G. Jorstad, Vladimir Karas, Takao Kitaguchi, Jeffery J.  
Kolodziejczak, Fabio La Monaca, Luca Latronico, Ioannis Liodakis, Simone Maldera, Alberto  
Manfreda, Frédéric Marin, Andrea Marinucci, Alan P. Marscher, Herman L. Marshall, Giorgio  
Matt, Ikuyuki Mitsuishi, Tsunefumi Mizuno, Stephen C.-Y. Ng, Stephen L. O'Dell, Chiara  
Oppedisano, Alessandro Papitto, George G. Pavlov, Abel L. Peirson, Matteo Perri, Melissa  
Pesce-Rollins, Maura Pilia, Juri Poutanen, Simonetta Puccetti, Brian D. Ramsey, Ajay Ratheesh,  
Roger W. Romani, Carmelo Sgrò, Patrick Slane, Paolo Soffitta, Gloria Spandre, Fabrizio  
Tavecchio, Yuzuru Tawara, Allyn F. Tennant, Nicholas E. Thomas, Francesco Tombesi, Alessio  
Trois, Sergey S. Tsygankov, Jacco Vink, Kinwah Wu, Fei Xie

Correspondence to: [taverna@pd.infn.it](mailto:taverna@pd.infn.it)

### This PDF file includes:

Materials and Methods  
Figs. S1 to S10  
Tables S1 to S3

## Materials and Methods

### Observations and data processing

The IXPE observatory includes three identical x-ray telescopes, each comprising an x-ray mirror assembly and a polarization-sensitive pixelated detector (31, 32), for measuring the energy, arrival direction, arrival time and linear polarization of the detected x-ray signal. We analyzed the data using software developed by the IXPE collaboration and collected in the IXPEOBSSIM suite (33) and independently with XSPEC (16), using the instrument response functions provided in the IXPE calibration Database [CALDB, (34)].

IXPE raw data consist of images of photoelectron tracks generated by X-ray photons absorbed in a gas cell. After downlinking to Earth, these were equalized by the gain of each detector pixel and then analyzed to calculate the absorption point of the photon, its energy and the direction of emission of the photoelectron, which is statistically related to the polarization of the absorbed photons (31, 32). All these quantities, stored in Level 1 files, were processed to apply calibrations and to project the photon incident direction and polarization angle onto the plane of the sky, to produce Level 2 files. Our analysis started from Level 2 data. We combine two 4U 0142+61 observations: the first started on 2022 January 31 at 07:37:07 Universal Time Coordinated (UTC) and ended on 2022 February 14 at 23:44:12 UTC, the second started on 2022 February 25 at 04:38:09 UTC and ended on 2022 February 27 at 18:46:09 UTC. The average net exposure time for the three telescopes was 835,719 seconds. We selected the source in the instrument field of view and identified a region for background subtraction using the SAOIMAGEDS9 software (35). The source counts were extracted from a circular region with radius  $46''$  and the background from a concentric annulus with inner and outer radius of  $106''$  and  $293''$ , respectively. The selected regions for each of the three IXPE DUs are shown in Figure S1A-C. Figure S1D shows the background for DU1 (representative of all the others); the background is uniform across the field of view. We then converted photon arrival times to the Solar System barycenter with the BARYCORR FTOOL included in HEASOFT 6.30.1 (16), using the object coordinates in the Flexible Image Transport System (FITS) files, the Jet Propulsion Laboratory (JPL) Development Ephemeris [DE421, see (36)] and the International Celestial Reference System (ICRS) reference frame.

Figure S2 shows the light curves of the source and of the background. Both were almost constant during the IXPE observation; therefore, we decided to join the two observations and analyze them as a single dataset.

### Timing analysis

We searched around the known rotation frequency of 4U 0142+61,  $f = 0.115092$  Hz (12), and in a range of frequency derivatives using a  $Z_n^2$ -search technique [see (37)]. We used the quasi-fast folding algorithm included in the HENDRICS software v.7.0 (38, 39), which is based on stingray 1.0 (40). We ran HENZSEARCH, initially using 16 bins for the pre-folding and accounting for one harmonic (i.e.  $n = 1$ , sinusoidal pulsations). Once we determined an initial solution around 0.115079 Hz, we found that the pulse profile was better described by at least 5 harmonics using the H-test (41). Hence, we re-ran the  $Z_n^2$ -search, this time using  $n = 5$  and 64

bins for pre-folding. Using the 90% confidence limits on the power (42, 43) [as adapted (44) and implemented in HENDRICS using STINGRAY.STATS], we determined the 68.3% confidence limit on the frequency  $f = 0.115079332 \pm 8 \times 10^{-9}$  Hz and on the frequency derivative  $\dot{f} = -(2.1 \pm 7) \times 10^{-14}$  Hz s<sup>-1</sup>. The corresponding contour plot of the statistical variable  $Z_n^2$  [defined in (37)] as a function of  $f$  and  $\dot{f}$  is reported in Figure S3. We further refined the results in the following way: using HENPHASEOGRAM, we split the observation into 32 intervals and calculated the times of arrival (TOAs) of the pulsations for each 10 intervals with the FFTFIT algorithm (45); then, we used the PINT software (46) to fit these TOAs with a spin-down model, obtaining final values of  $f = 0.115079336 \pm 6 \times 10^{-9}$  Hz and  $\dot{f} = -(2.1 \pm 0.7) \times 10^{-14}$  Hz s<sup>-1</sup>.

### Spectral analysis

Spectral analysis was carried out with the python interface to the x-ray spectral-fitting package XSPEC, version 12.12.1 (16). Interstellar absorption was taken into account by using the XSPEC model `tbabs` with standard abundances (47). Due to the limited energy resolution and energy range of the IXPE data, we tested only three simple models:

1. `tbabs × (bbody+powerlaw)`, which has previously been applied to 4U 0142+61 (18),
2. `tbabs × (bbody+bbody)`, which has also been applied to magnetars [see e.g. (3)]
3. `tbabs × (bbody+trcpow)`, where `trcpow` is a truncated power-law, that is, a power-law which drops to zero below an energy threshold,  $E_{\text{trc}}$ . We introduce this model to mimic a physical picture in which the power law is produced at the expenses of low energy photons, like in the RCS scenario, and so it does not extend below a few keVs.

We found that the absorption component is unconstrained, due to the lack of IXPE sensitivity below 2 keV. Therefore, we fixed the interstellar, hydrogen column density  $n_{\text{H}}$  to the value found by a previous analysis (17),  $n_{\text{H}} = 0.57 \times 10^{22}$  cm<sup>-2</sup>. This value is lower but compatible with a previous measurement (48),  $n_{\text{H}} = 0.64 \times 10^{22}$  cm<sup>-2</sup> and a broadband analysis (21) which found values in the range  $\sim 0.5\text{--}1.3 \times 10^{22}$  cm<sup>-2</sup>, depending on the assumed spectral model.

The models were fitted to the spectra from all three IXPE telescopes simultaneously, allowing for an energy-independent cross-normalization factor for the second and third detectors to account for the uncertainties in their absolute effective area calibration. The results of the background-subtracted spectral fitting in the energy interval 2–8 keV are reported in Table S1 and shown in Figure S4. The  $\chi^2$  of the `bbody+powerlaw` and the `bbody+bbody` models are 511.5 and 496.0, respectively, for 441 degrees of freedom. The best fitting parameters obtained for the `bbody+powerlaw` model are close to those derived in previous observations (18), although the temperature and the photon index are not formally consistent at  $1\sigma$  level. This is at least partially related to the different value adopted for  $n_{\text{H}}$ . The unabsorbed flux for DU1 (which is taken as a reference) is  $\sim 6.5 \times 10^{-11}$  erg s<sup>-1</sup> cm<sup>-2</sup> in the 2–10 keV energy range. Cross-normalization factors  $w$ 's are within 15%, which is common for x-ray missions (49), especially in their early phases.

The `bbody+trcpow` model has residuals at low energy that can mostly be removed by making the column density a free parameter. We instead keep it fixed, and use this spectral model only for the joint spectro-polarimetric analysis, discussed below.

We performed a phase-resolved spectral analysis, grouping the data in six phase bins; because there are insufficient counts at high energies, we considered only the 2–7 keV range. The obtained spectra are shown in Figure S5A, where the selected phases are also reported. The best fitting parameters for the `w×tbabs×(bbody+powerlaw)` model are shown in Figure S5B. No statistically significant spectral changes with phase were detected.

### Polarization analysis

Polarization analysis was carried out with two different methods. The first uses the tools available in IXPEOBSSIM (33). This model-independent polarization analysis is based on an unbinned procedure described elsewhere (50). While a weighted analysis can provide an increase in sensitivity (51, 52), no appropriate software was available. We therefore used the simpler unweighted procedure. Stokes parameters were calculated event-by-event from the photoelectron track emission angle and calibrated for the known spurious modulation of the instrument (53). Because the Stokes parameters are additive (50), those for each energy band were obtained by simply summing the parameters of all the events in the energy range of interest. Background removal was performed by subtracting its contribution from the Stokes parameter fluxes of the source.

The second approach used the XSPEC spectral fitting package following published methodology (54). Event-by-event Stokes parameters, already calibrated for the spurious modulation (50), were binned in energy to produce three independent spectra for  $I$ ,  $Q$ , and  $U$ ; the latter were then fitted jointly with the XSPEC procedure of forward folding. The polarization instrumental response is accounted for by the modulation response function, taken from the IXPE CALDB. The background was removed in each energy bin by subtracting from the source Stokes spectra the corresponding background spectra, after rescaling the number of background counts to the area of the source extraction region. Polarization in each bin was calculated by assuming the `tbabs×(bbody+powerlaw)` model with parameters fixed to those obtained by the spectral analysis above, then convolved with the constant polarization model `polconst` provided by XSPEC. Only the polarization degree and angle are left as free parameters; the polarization in different energy bands is obtained by restricting the Stokes spectra to the energy channel of interest.

For both analyses, the subtraction of the spurious modulation and of the background has a minor impact on the source signal. We compare the (unnormalized) Stokes spectra of the three components in Figure S6. Spurious modulation is apparent only at lower energies, where the source polarization is much larger and detected with high significance. The background becomes non-negligible at higher energies, but it is largely unpolarized, so its Stokes parameters are negligible with respect to those of the source.

The results of the separate analysis of the three IXPE detectors, for both the IXPEOBSSIM and XSPEC methods, are reported in Table S2 in each energy band. In Table S2 we report the  $1\sigma$  (68.3% confidence level) statistical uncertainty on both PD and PA calculated following

published methods (50), under the assumptions that Stokes parameters are normally distributed and correlated, and that PD and PA are independent. When the measured PD is lower than the MDP<sub>99</sub> (55), we list only the latter as an upper limit; for PA, instead, we report the best-fitting value and extend the uncertainty interval over the entire range,  $PA - 90^\circ$ – $PA + 90^\circ$ .

5 Uncertainties for the XSPEC analysis are derived with the `error` command of XSPEC for each parameter of interest.

The polarization degree and angle are not truly independent (especially for low-significance measurements). For this reason, we also determined the 68.3% confidence level for the joint measurement of the polarization degree and angle (shown in Figure 2). In the IXPEOBSSIM analysis, this is derived with standard functions (55–57) from the measured quantities. This approach assumes that the Stokes parameters are normally distributed and uncorrelated, which is a good approximation for the polarization degree exhibited by 4U 0142+61 and for the IXPE modulation factor in the 2–8 keV energy range. For the XSPEC analysis, we used the `steppar` command to determine the contour regions, assuming two parameters of interest. Figure S7 shows the normalized Stokes parameters measured in the five energy bands considered in our analysis.

We also performed a joint spectro-polarimetric analysis with XSPEC, fitting the Stokes spectra  $I$ ,  $Q$  and  $U$  simultaneously with models which account for the energy dependence both in the spectral and polarization properties. We started from the three models discussed above for the spectral analysis, then associated each additive component with a different polarization, assumed to be constant with energy. The interstellar column density and cross-calibration of the three detectors were fixed at the same values as the spectral analysis (Table S1), while all the other parameters were free parameters. The results of this analysis are shown in Figures S7–S9 and parameters are reported in Table S3.

25 We find that the spectral parameters agree with those found in the spectral analysis above, within the statistical uncertainties. This indicates that the adopted spectral decomposition is consistent with the polarization analysis, so likely reflects a different physical origin for the two components, each characterized by its own spectral and polarization properties. The polarization degree of the two components is strongly model dependent; for example, the low-energy blackbody has a polarization of  $\sim 60\%$  when the model also contains a power-law, but  $\sim 17\%$  when the second component is a truncated power law. This is because the two models imply a different contribution of the high-energy component at low energies and therefore their polarization must adjust so that their sum matches the observed polarization. The results obtained with the `tbabs*(bbody+trcpow)` model are less affected by this issue and therefore we prefer them over the other models. Nonetheless, in all cases we observe a swing of the polarization angle by  $90^\circ$  between the two components, which is therefore a robust feature.

### Variation of PA with phase and the rotating vector model

The phase-dependent analysis above showed that the polarization angle as a function of the rotational phase is consistent with the rotating vector model [RVM; (20, 58)]. RVM provides a simple method to compute the polarization angle of radiation coming from a small (point-like) region located at (or close to) the magnetic pole of a neutron star. If the neutron star magnetic field is a dipole (so  $B$  at the emitting point is along the magnetic axis), the angle between the

projection of the field in the plane of the sky and a reference direction, taken as the projection in the same plane as the spin axis, is given by (58):

$$\tan \alpha = \frac{\sin \xi \sin \gamma}{\cos \chi \sin \xi \cos \gamma - \sin \chi \cos \xi} \quad (\text{S1})$$

where  $\chi$  and  $\xi$  are the inclinations of the observer's line-of-sight and the star dipole axis with respect to the spin axis, and  $\gamma$  is the rotational phase. The angle  $\alpha$  coincides with the polarization angle PA.

If radiation comes from an extended region, the situation is more complicated. Because the direction of  $B$  changes substantially on the surface,  $\alpha$  is different at the different emission points. The PA is then (10):

$$\tan(2\text{PA}) = \frac{\sum_i^{N_X} \sin(2\alpha_i) - \sum_i^{N_O} \sin(2\alpha_i)}{\sum_i^{N_O} \cos(2\alpha_i) - \sum_i^{N_X} \cos(2\alpha_i)} \quad (\text{S2})$$

where the two summations are over the total number of X ( $N_X$ ) or O ( $N_O$ ) mode photons, the index  $i$  runs over the number of photons and

$$\tan \alpha_i = -\frac{B_{y,i}}{B_{x,i}} \quad (\text{S3})$$

where  $B_{y,i}$ ,  $B_{x,i}$  are the (Cartesian) components of the (local) magnetic field in the plane of the sky. If all the  $\alpha_i$  are equal to the same value,  $\alpha$ , this leads to  $\text{PA} = \alpha$ . Although this is not generally true for emission coming from the surface, it becomes so if the polarization direction is determined by the properties on a sphere of radius much larger than the neutron star radius. At great distances from the neutron star, the dipolar field direction changes little from point to point, so  $\tan \alpha_i$  is approximately the same for all photons. The common value  $\alpha$  is then given by equation S1. The Cartesian components of the field perpendicular to the line-of-sight are related to those referred to the dipole axis by:

$$\begin{aligned} B_x &= B_p p_x + B_q q_x + B_t t_x \\ B_y &= B_p p_y + B_q q_y + B_t t_y \end{aligned} \quad (\text{S4})$$

where the subscripts  $p$ ,  $q$  and  $t$  indicate the axes unit vectors, with  $t$  along the dipole axis. By relating  $B_p$ ,  $B_q$  and  $B_t$  to the polar components of the dipole field and summing over the entire surface, only the  $t$  contribution survives in equations S4, with  $t_y$  and  $t_x$  given by the numerator and denominator of equation S1 (10).

We expect vacuum birefringence to force the photon polarization vectors to align with the magnetic field up to the polarization-limiting radius ( $r_{pl}$ ), which is typically  $\sim 100$  stellar radii for a magnetar (7, 11). This would cause the observed polarization degree to be close to that at the original emission. However, following the change in direction of the polarization vectors, the polarization angle would change continuously until photons arrive at  $r_{pl}$ , where the polarization vectors stop changing. For 4U 0142+61, this is consistent with the observed phase-dependent behavior of PD and PA, with the former resembling the double-peaked profile of the flux, while

the latter is consistent with the RVM. Given the large degeneracy of the parameters in equation (S1), it was not possible to obtain a precise value for the angles  $\chi$  and  $\xi$  from the fit.

### Numerical modeling

5 Results of the numerical simulation shown in Figure 2 were obtained with the code described in (7). Thermal photons are emitted by the condensed surface layers of the NS, assuming a Fe composition and in the fixed-ion approximation for the dielectric tensor of the solid [(23); this means that ions in the lattice do not move in response to an incident  
10 electromagnetic wave]. The energy, direction and polarization state of each photon is then upgraded as it undergoes repeated scatterings onto electrons flowing in the magnetosphere until it reaches the observer. Quantum electrodynamical effects are accounted for by integrating the wave equation along the photon path as discussed in (7, 9). The Stokes parameters of individual photons are finally collected as function of energy and direction. Spectra are obtained by  
15 summing together the contribution of the part in view of the NS and averaging over the rotational phase. Simulations have been performed for a large range of inclination angles  $\chi$  and  $\xi$ , as well as for different values of the magnetospheric twist angle  $\Delta\phi$ , the velocity  $\beta$  (in units of the speed of light) that characterizes the charge motion along the closed field lines and the surface temperature  $kT_s$  [see (7) for more details]. The results shown in Figure 2 refer to the simulation  
20 which provided the closest match with the IXPE data, corresponding to  $\Delta\phi = 0.1$  rad,  $\beta = 0.5$ ,  $kT_s = 0.5$  keV and  $\chi = 40^\circ$ ,  $\xi = 30^\circ$ . In the present case a total of  $\sim 10^7$  photons were launched. We set the NS magnetic field strength to  $4 \times 10^{14}$  G at the pole so to match the strength at the equator inferred from the timing analysis of IXPE data. The emitting zone was limited to an axisymmetric region about the magnetic equator, with opening angle  $\Theta = 36^\circ$ .

### Comparing the measured and the simulated polarization angle

25 Our numerical simulations within the RCS scenario produce the Stokes parameters of the source, from which the polarization degree and angle are derived. Care must be taken when comparing the results for the polarization angle with observations. In our calculations PA is counted from the projection of the NS spin axis in the plane of the sky, since in this way PA is  $0^\circ$  ( $90^\circ$ ) for O (X) mode photons [see (10)]. However, the direction from which PA is measured by  
30 the instrument does not necessarily coincide with the spin axis projection. In the general case in which the spin axis projection makes an angle  $\psi$  with the instrument reference direction, the polarization angle of O-mode photons turns out to be  $\psi$  or  $90^\circ + \psi$  in the case of X-mode photons. The angle  $\psi$  is a free parameter of the model and can be adjusted to match observations. This is the reasoning at the basis of argument we put forward about the association between the  
35 spin axis direction and the polarization angle.

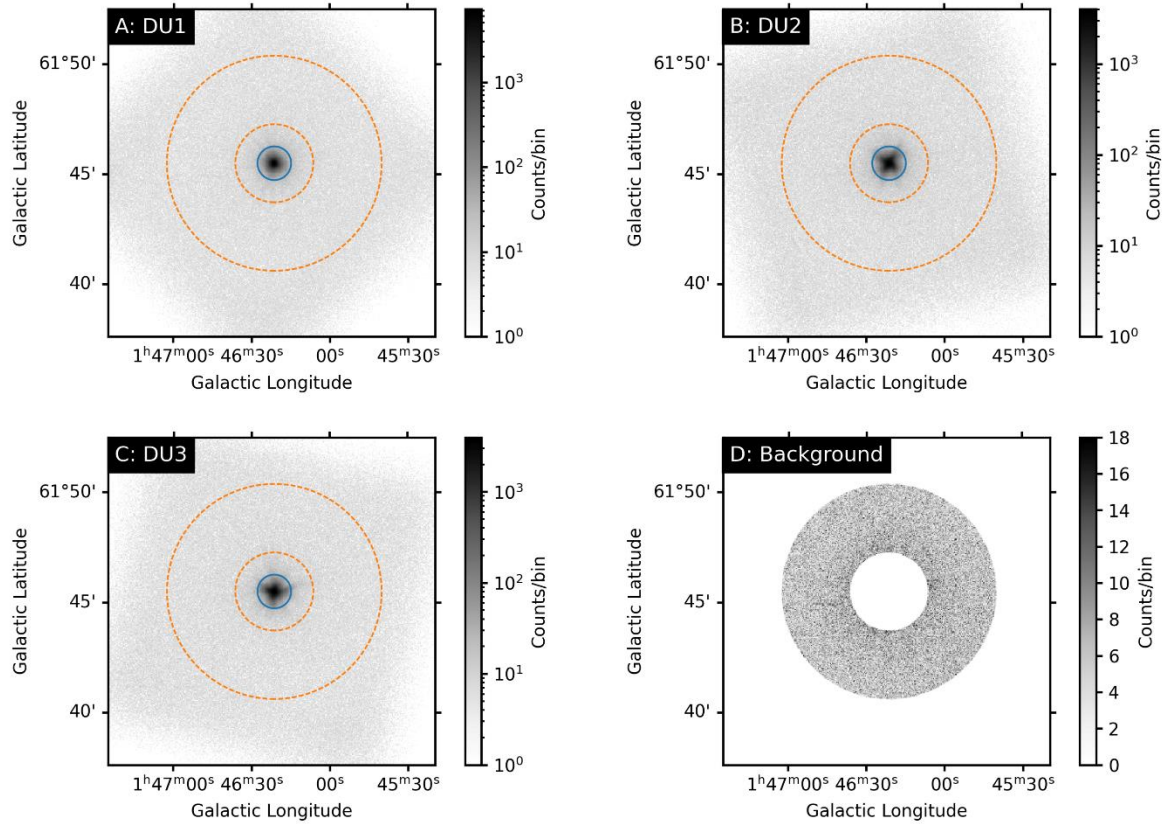


**Fig. S1. Source and background regions selected with SAOIMAGEDS9.**

(A to C) the selected source (solid blue circle) and background (dashed orange circles) regions, for DU1 to DU3 shown on a logarithmic scale. (D) The background for DU1, which is representative of all the DUs, shown on a linear scale.

5

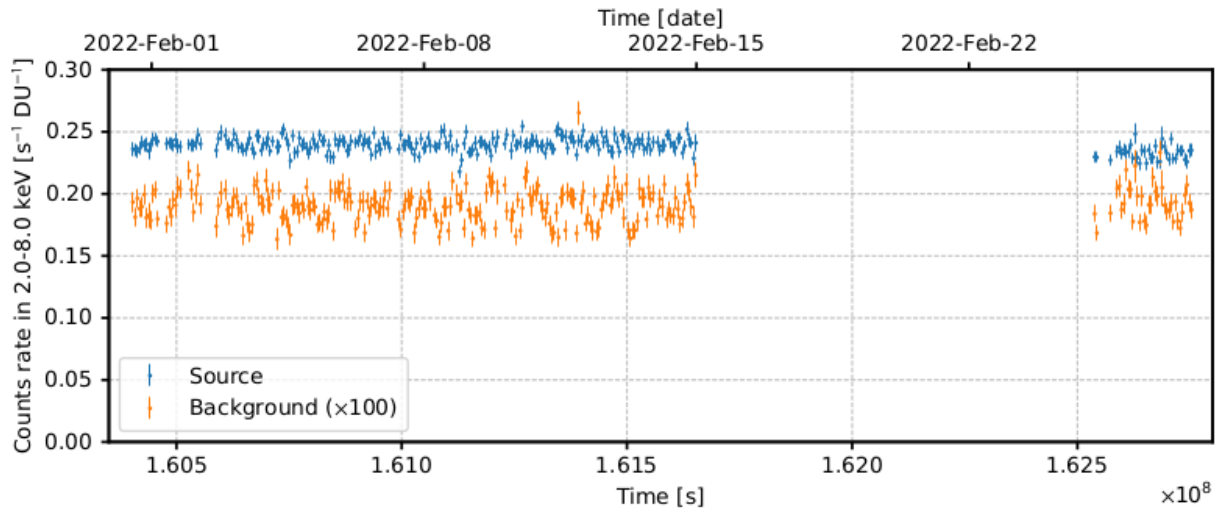


**Fig. S2. Light curve of the source and of the background during the two IXPE observations of 4U 0142+61.**

5 Both the source (blue) and the background (orange) were almost constant, so we analyzed the two observations as a single dataset. The background rate is rescaled in such a way the extraction area of the background region is the same as that of the source and was multiplied by a factor of 100 for display. Values are averaged over the three DUs and errors are at  $1\sigma$ .

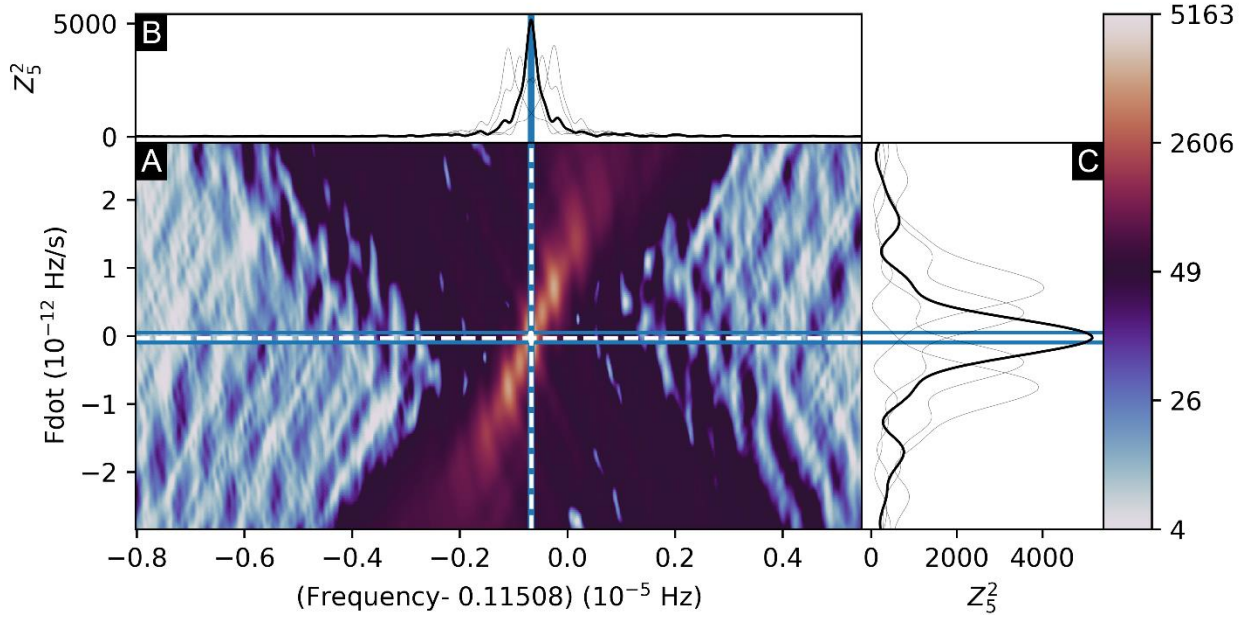


**Fig. S3.  $f$ - $\dot{f}$  diagram for the IXPE observations of 4U 0142+61.**

(A) the values of the  $Z_n^2$  statistical variable for  $n = 5$  [see (37)] plotted as a function of  $f$  and  $\dot{f}$ . Dashed white lines indicate the best  $f$  and  $\dot{f}$  values found in the analysis, while solid blue lines indicate the contours of 90 % confidence of the maximum power (see the text for details). (B and C) constant- $\dot{f}$  and constant- $f$  cuts of panel A corresponding to the best (solid black lines) and the next four (solid gray lines)  $f$  and  $\dot{f}$  candidates.

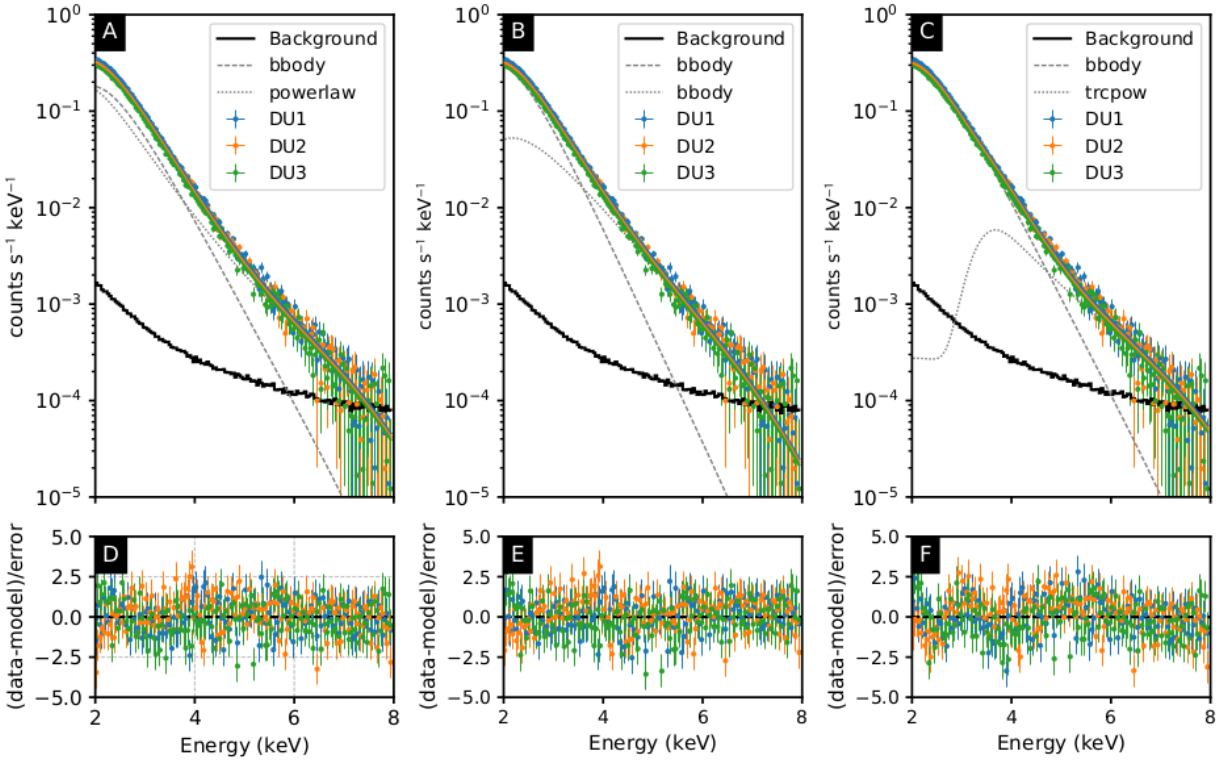


**Fig. S4. Spectral fitting of the total IXPE counts.**

Data (cyan, orange and green points with error bars, at  $1\sigma$  level) for DU1, DU2 and DU3. (A to C) best fit model  $tbabs \times (bbody + powerlaw)$ ,  $tbabs \times (bbody + bbody)$  and  $tbabs \times (bbody + trcpow)$  (cyan, orange and green solid lines for DU1, DU2 and DU3). The two additive components of each model (gray dashed and dotted lines) and the average background counts (black solid line) are also shown. (D to F) corresponding normalized residuals.

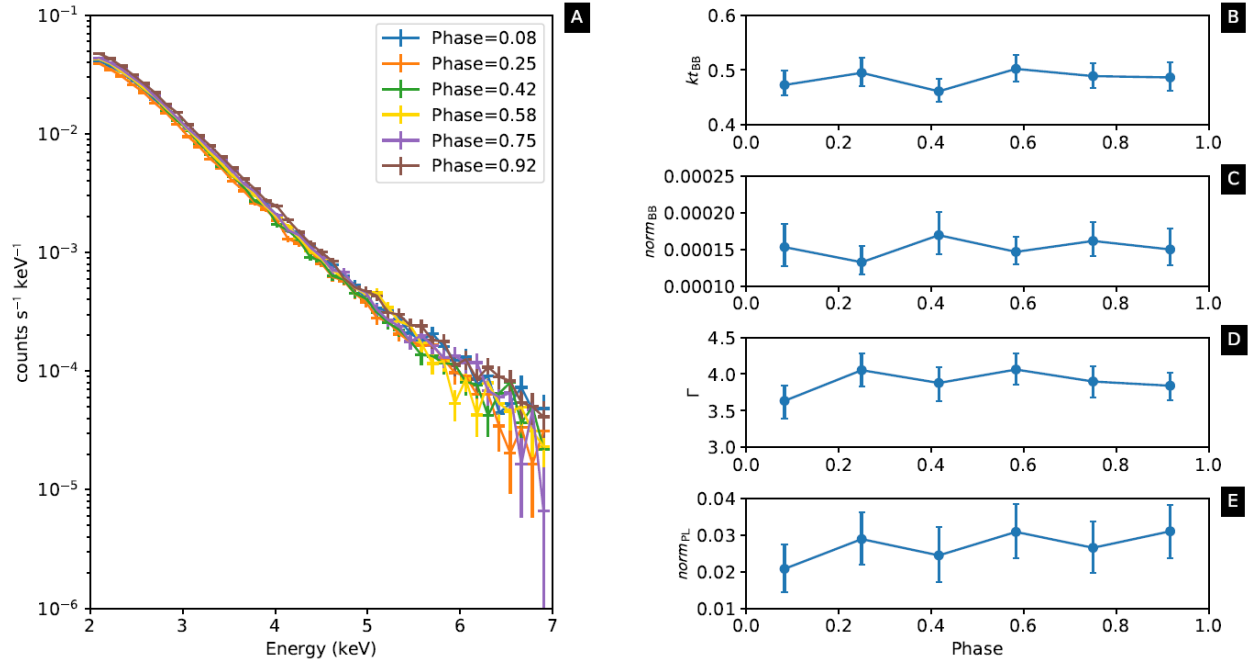


**Fig. S5. Phase-resolved spectral analysis of 4U 0142+61.**

(A) spectra obtained by folding the data at the measured spin period and grouping them in six, equally-spaced phase intervals. (B to E): phase-dependent behavior of the blackbody temperature ( $kT_{BB}$ ) and normalization ( $norm_{BB}$ ), power-law photon index ( $\Gamma$ ) and normalization ( $norm_{PL}$ ) obtained by fitting the spectrum in each phase bin with the  $w \times tbabs \times (bbody + powerlaw)$  model (cf. Figure S4A). Errors are given at  $1\sigma$  confidence level. Phases refer to the center of each bin.

5

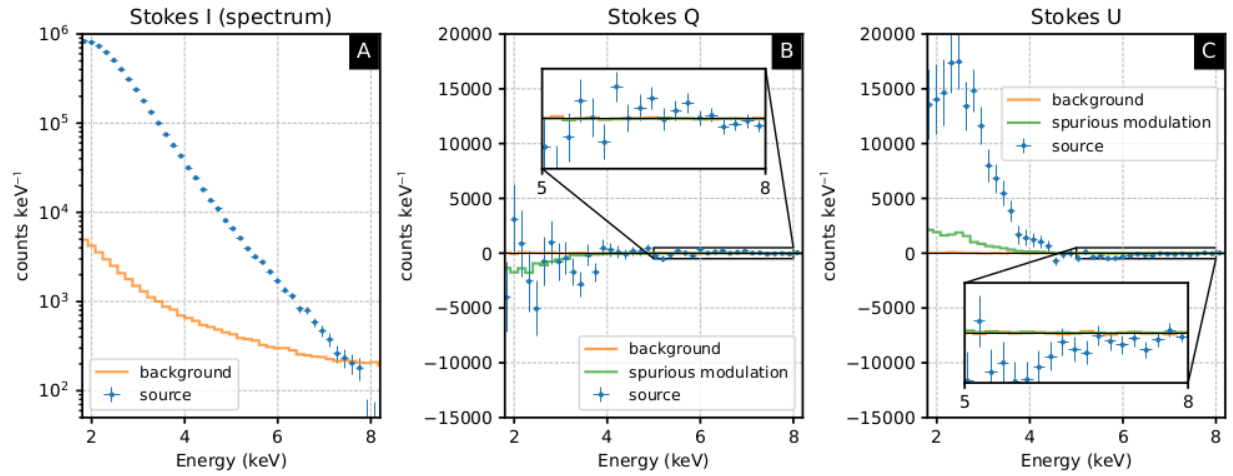


**Fig. S6 Comparison of the Stokes spectra of the source with those of the spurious modulation and background.**

(A to C) spectra of the Stokes parameters  $I$ ,  $Q$  and  $U$  for the source (cyan points with error bars, at  $1\sigma$  level) and the background (orange solid line). Insets in panels B and C are zooms. Spurious modulation (green solid line) is reported in panels B and C and is determined by summing the contributions of the three detectors, accounting for their relative orientation with respect to the sky. Source spectra are spurious modulation and background subtracted. The  $I$  spectrum of the spurious modulation coincides with that of the source.

5

10

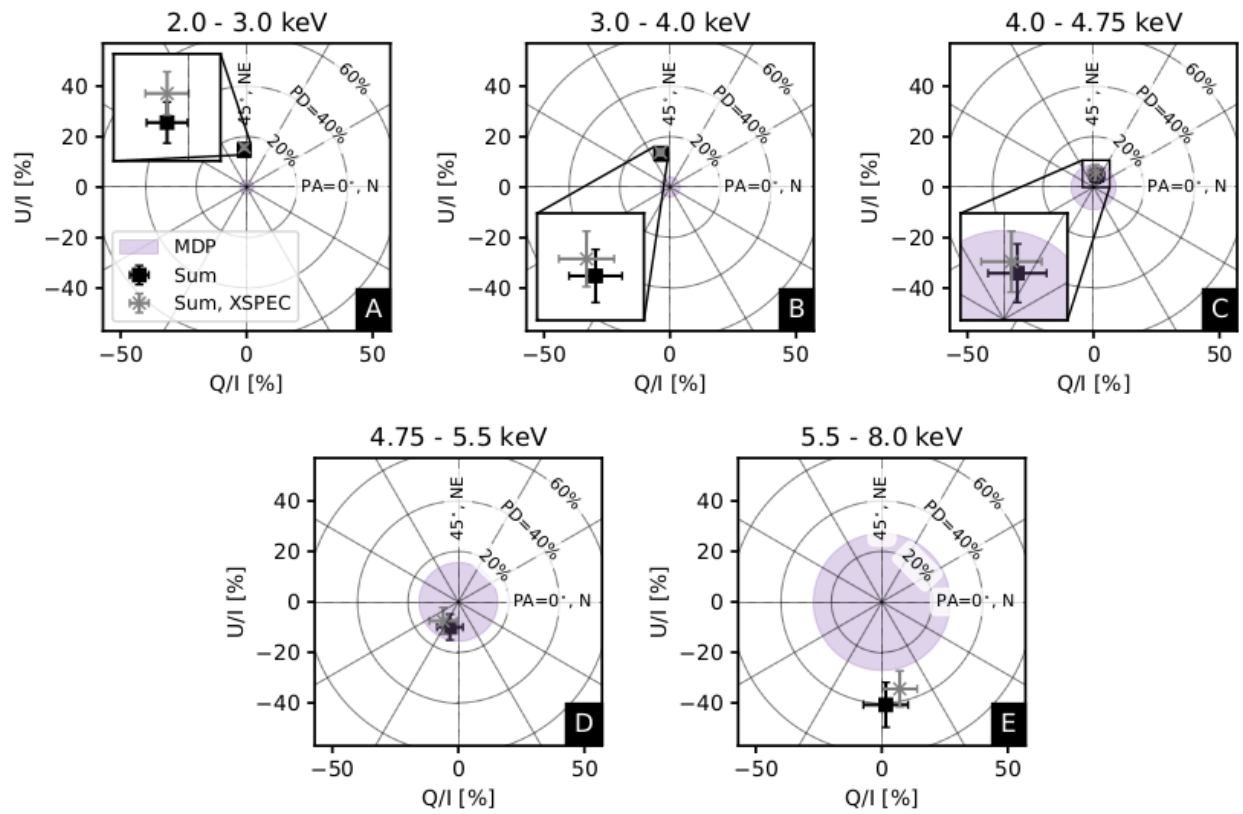


**Fig. S7. Energy-dependent normalized Stokes parameters.**

(A to E) Black squares (gray crosses) with  $1\sigma$  error bars indicate the combined  $Q/I$  and  $U/I$  derived with IXPEOBSSIM (XSPEC) in the same energy bins as in Fig. 2. Insets in panels A to C are zooms. Lines and purple shading are as in Figure 1. Data were background-subtracted.

5

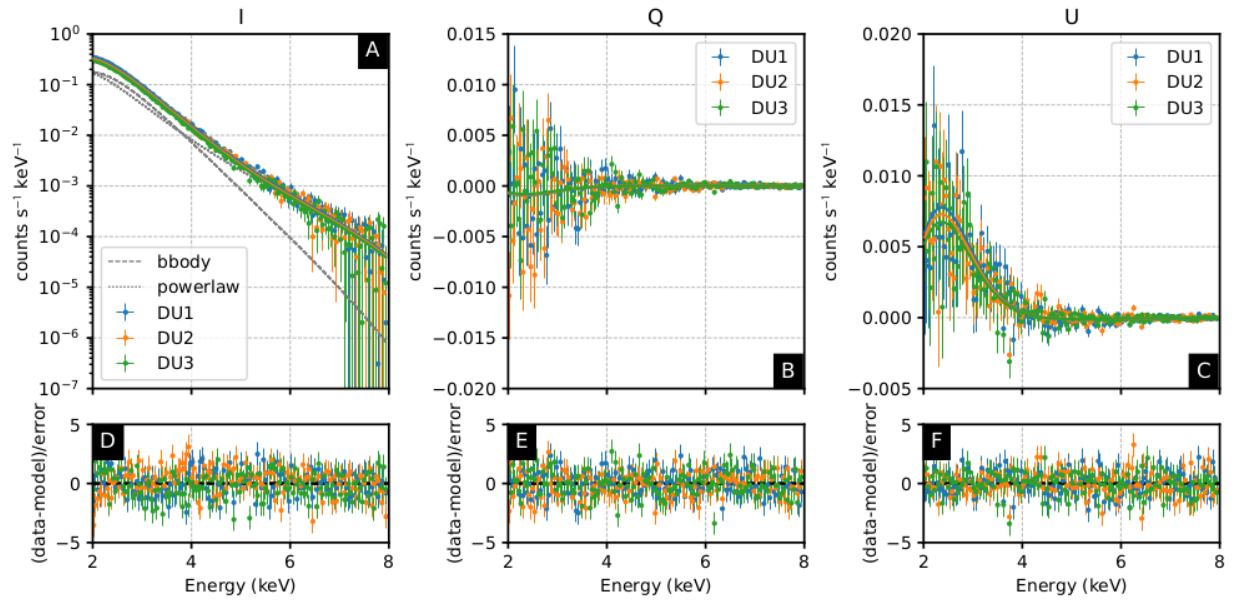


**Fig. S8.** Same as Figure S4, but for the spectro-polarimetric model  $\text{tbabs} \times (\text{bbody} \times \text{polconst} + \text{powerlaw} \times \text{polconst})$ .

5 Best fitting parameters are reported in Table S3.

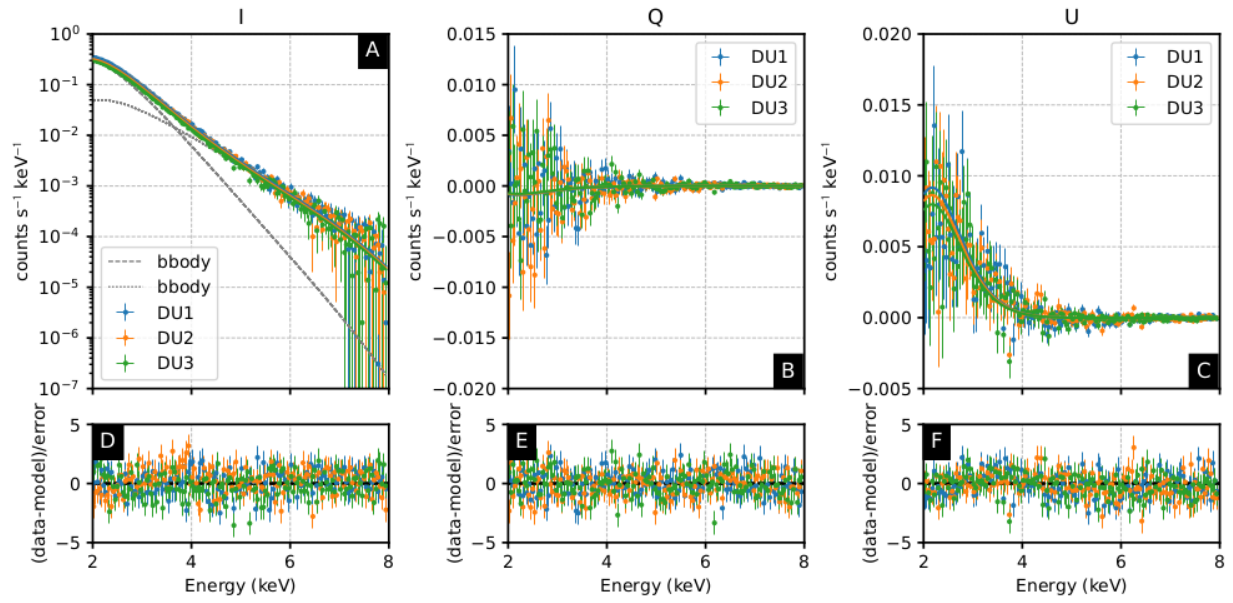


**Fig. S9.** Same as Figure S8, but for spectro-polarimetric model  $\text{tbabs} \times (\text{bbody} \times \text{polconst} + \text{bbody} \times \text{polconst})$ .

5 Best fitting parameters are reported in Table S3.

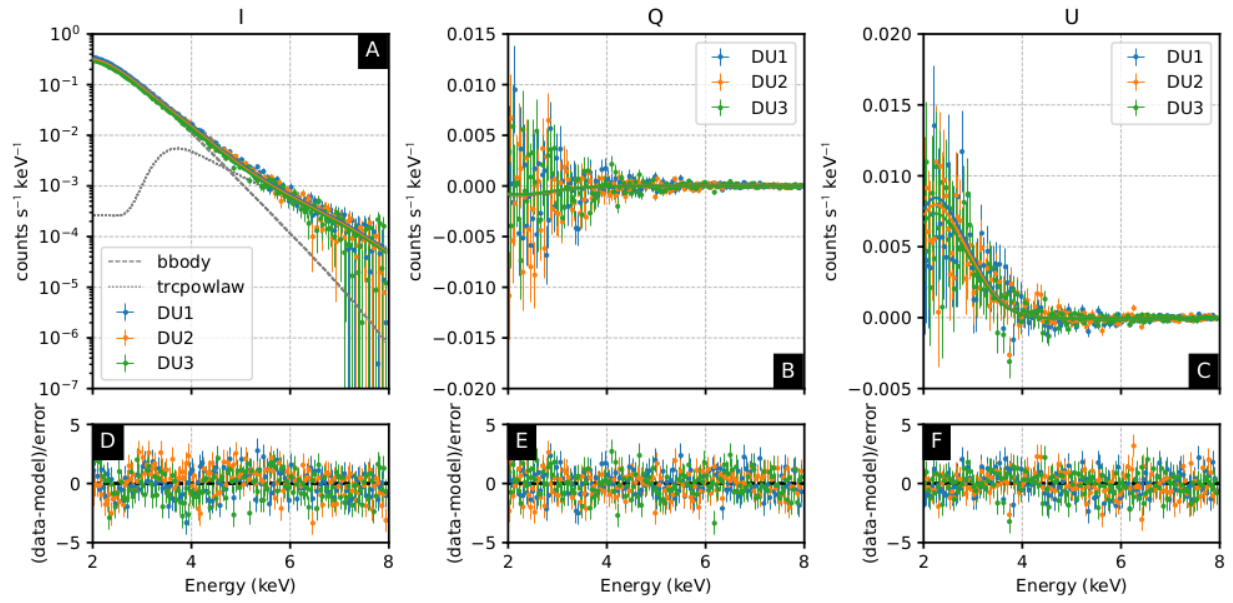


**Fig. S10. Same as Figure S8, but for the spectro-polarimetric model  $\text{tbabs} \times (\text{bbody} \times \text{polconst} + \text{trcpow} \times \text{polconst})$ .**

Best fitting parameters are reported in Table S3.

**Table S1. Results of fitting the spectral models to the IXPE data.**

The values of  $n_H$  and of the constant factor  $w_{DU1}$  are fixed parameters.  $kT_{BB}$  indicates the temperature of the blackbody component for the models  $w \times tbabs \times (bbody + powerlaw)$  and  $w \times tbabs \times (bbody + trcpow)$ , while  $kT_{BB1}$  and  $kT_{BB2}$  are the temperature of the first and second blackbody components, respectively, for the model  $w \times tbabs \times (bbody + bbody)$ . The blackbody normalization fitting parameters  $norm_{BB}$ ,  $norm_{BB1}$  and  $norm_{BB2}$  are defined as  $L/D^2$  where the source luminosity  $L$  and distance  $D$  are in units of  $10^{39}$  erg  $s^{-1}$  and 10 kpc, respectively. The power-law normalization fitting parameter  $norm_{PL}$  is in units of counts  $keV^{-1} cm^{-2} s^{-1}$  at 1 keV.  $E_{trc}$  indicates the truncated power-law energy threshold. Uncertainties are at 68.3% confidence level. The number of degrees of freedom is 441 in the fit with the  $w \times tbabs \times (bbody + powerlaw)$  and  $w \times tbabs \times (bbody + bbody)$  models, and 440 with the  $w \times tbabs \times (bbody + trcpow)$  model.

w × tbabs × (bbody + powerlaw)									
$n_H$ $10^{22} cm^{-2}$	$kT_{BB}$ keV	$norm_{BB}$ $\times 10^{-3}$	$\Gamma$	$norm_{PL}$ $\times 10^{-1}$	$w_{DU1}$	$w_{DU2}$ $\times 10^{-1}$	$w_{DU3}$ $\times 10^{-1}$	$\chi^2$	
0.57	$0.471^{+0.004}_{-0.004}$	$1.08^{+0.04}_{-0.03}$	$3.69^{+0.05}_{-0.05}$	$1.19^{+0.08}_{-0.08}$	1.0	$9.63^{+0.03}_{-0.03}$	$8.55^{+0.03}_{-0.03}$	511.5	
w × tbabs × (bbody + bbody)									
$n_H$ $10^{22} cm^{-2}$	$kT_{BB1}$ keV	$norm_{BB1}$ $\times 10^{-3}$	$kT_{BB2}$ keV	$norm_{BB2}$ $\times 10^{-3}$	$w_{DU1}$	$w_{DU2}$ $\times 10^{-1}$	$w_{DU3}$ $\times 10^{-1}$	$\chi^2$	
0.57	$0.399^{+0.004}_{-0.004}$	$1.96^{+0.01}_{-0.01}$	$0.81^{+0.02}_{-0.02}$	$0.40^{+0.02}_{-0.02}$	1.0	$9.63^{+0.03}_{-0.03}$	$8.55^{+0.03}_{-0.03}$	496.0	
w × tbabs × (bbody + trcpow)									
$n_H$ $10^{22} cm^{-2}$	$kT_{BB}$ keV	$norm_{BB}$ $\times 10^{-3}$	$\Gamma$ keV	$norm_{PL}$ $\times 10^{-1}$	$E_{trc}$ keV	$w_{DU1}$	$w_{DU2}$ $\times 10^{-1}$	$w_{DU3}$ $\times 10^{-1}$	$\chi^2$
0.57	$0.447^{+0.001}_{-0.001}$	$2.07^{+0.01}_{-0.01}$	$2.69^{+0.06}_{-0.04}$	$0.28^{+0.01}_{-0.02}$	$3.340^{+0.058}_{-0.002}$	1.0	$9.63^{+0.03}_{-0.03}$	$8.55^{+0.02}_{-0.02}$	586.2

**Table S2. Measured polarization degree and angle at different energies.**

Polarization degree and angle measured with the three IXPE DUs separately and combined using the model-independent analysis [(50), as implemented in IXPEOBSSIM] and XSPEC. Uncertainties are 68.3% confidence level, assuming that the polarization degree and angle are independent.

5 When the measured value of the polarization degree is lower than  $MDP_{99}$ , we show the latter as an upper limit and assume that the polarization angle can vary over its entire range. Signal-to-noise ratio (S/N) is calculated by dividing the XSPEC combined polarization degree by its uncertainty.

	2-3 keV	3-4 keV	4-4.75 keV	4.75-5.5 keV	5.5-8 keV	2-8 keV
PD - DU1 [%]	$13.2^{+1.6}_{-1.6}$	$15.1^{+2.2}_{-2.2}$	< 14.9	< 25.8	< 44.5	$11.2^{+1.3}_{-1.3}$
PD - DU2 [%]	$15.0^{+1.6}_{-1.6}$	$12.5^{+2.2}_{-2.2}$	< 15.5	< 26.5	$46.5^{+15.3}_{-15.3}$	$12.5^{+1.4}_{-1.4}$
PD - DU3 [%]	$15.9^{+1.7}_{-1.7}$	$12.7^{+2.4}_{-2.4}$	< 16.3	< 29.1	$52.9^{+16.7}_{-16.7}$	$12.0^{+1.5}_{-1.5}$
PD - IXPEOBSSIM [%]	$14.5^{+0.9}_{-0.9}$	$13.4^{+1.3}_{-1.3}$	< 9.0	< 15.6	$40.8^{+8.9}_{-8.9}$	$11.8^{+0.8}_{-0.8}$
PD - XSPEC [%]	$15.8^{+1.0}_{-1.0}$	$14.3^{+1.4}_{-1.4}$	< 9.0	< 15.6	$35.2^{+7.1}_{-7.1}$	$13.5^{+0.8}_{-0.8}$
PD - XSPEC S/N	$15.8\sigma$	$10.2\sigma$	–	–	$5.0\sigma$	$16.9\sigma$
PA - DU1 [deg]	$46.0^{+3.4}_{-3.4}$	$48.1^{+4.2}_{-4.2}$	$-15.1^{+105.1}_{-74.9}$	$-33.2^{+123.2}_{-56.8}$	$-47.4^{+137.4}_{-42.6}$	$45.9^{+3.4}_{-3.4}$
PA - DU2 [deg]	$52.1^{+3.1}_{-3.1}$	$53.9^{+5.1}_{-5.1}$	$47.2^{+42.8}_{-137.2}$	$-71.4^{+161.4}_{-18.6}$	$-43.6^{+9.3}_{-9.3}$	$53.1^{+3.1}_{-3.1}$
PA - DU3 [deg]	$42.4^{+3.0}_{-3.0}$	$56.6^{+5.4}_{-5.4}$	$33.9^{+56.1}_{-123.9}$	$-69.8^{+159.8}_{-20.2}$	$-42.2^{+8.9}_{-8.9}$	$45.3^{+3.5}_{-3.5}$
PA - IXPEOBSSIM [deg]	$46.9^{+1.9}_{-1.9}$	$52.4^{+2.8}_{-2.8}$	$36.7^{+53.3}_{-126.7}$	$-54.2^{+144.2}_{-35.8}$	$-43.9^{+6.2}_{-6.2}$	$48.3^{+1.9}_{-1.9}$
PA - XSPEC [deg]	$46^{+1.8}_{-1.8}$	$52.8^{+2.8}_{-2.8}$	$41.2^{+48.8}_{-131.2}$	$-64.4^{+154.4}_{-25.6}$	$-39.2^{+5.7}_{-5.7}$	$48.5^{+1.6}_{-1.6}$

**Table S3. Results of fitting the spectro-polarimetric model to the IXPE data.**

The interstellar column density  $n_{\text{H}}$  and the constant factors  $w_{\text{DU1}}$ ,  $w_{\text{DU2}}$  and  $w_{\text{DU3}}$  were fixed to the values reported in the spectral analysis (table S1). All the other parameters are the same as in Table S1, with the exception of the polarization degree (PD) and angle (PA) of the constant polarization model. Uncertainties are at 68.3% confidence level marginalized over the parameter of interest. The number of degrees of freedom is 1333 in the fit with the

$w \times \text{tbabs} \times (\text{bbody} \times \text{polconst} + \text{powerlaw} \times \text{polconst})$  and  $w \times \text{tbabs} \times \text{bbody} \times \text{polconst} + \text{bbody} \times \text{polconst}$  models, and 1332 with the  $w \times \text{tbabs} \times \text{bbody} \times \text{polconst} + \text{trcpow} \times \text{polconst}$  model.

w×tbabs×(bbody×polconst+powerlaw×polconst)									
$kT_{\text{BB}}$ keV	norm <sub>BB</sub> × 10 <sup>-3</sup>	PD <sub>BB</sub>	PA <sub>BB</sub> deg	Γ	norm <sub>PL</sub> × 10 <sup>-1</sup>	PD <sub>PL</sub>	PA <sub>PL</sub> deg	χ <sup>2</sup>	
0.473 <sup>+0.004</sup> <sub>-0.004</sub>	1.06 <sup>+0.03</sup> <sub>-0.03</sub>	0.59 <sup>+0.06</sup> <sub>-0.06</sub>	48.0 <sup>+2.5</sup> <sub>-2.5</sub>	3.72 <sup>+0.04</sup> <sub>-0.05</sub>	1.23 <sup>+0.08</sup> <sub>-0.08</sub>	0.39 <sup>+0.07</sup> <sub>-0.06</sub>	-42.3 <sup>+4.3</sup> <sub>-4.3</sub>	1337.8	
w×tbabs×(bbody×polconst+bbody×polconst)									
$kT_{\text{BB1}}$ keV	norm <sub>BB1</sub> × 10 <sup>-3</sup>	PD <sub>BB1</sub>	PA <sub>BB1</sub> deg	$kT_{\text{BB2}}$	norm <sub>BB2</sub> × 10 <sup>-3</sup>	PD <sub>BB1</sub>	PA <sub>BB2</sub> deg	χ <sup>2</sup>	
0.401 <sup>+0.003</sup> <sub>-0.004</sub>	1.96 <sup>+0.01</sup> <sub>-0.01</sub>	0.23 <sup>+0.02</sup> <sub>-0.02</sub>	47.3 <sup>+2.1</sup> <sub>-2.1</sub>	0.82 <sup>+0.02</sup> <sub>-0.02</sub>	0.38 <sup>+0.02</sup> <sub>-0.02</sub>	0.06 <sup>+0.03</sup> <sub>-0.03</sub>	-50.8 <sup>+16.4</sup> <sub>-15.9</sub>	1360.4	
w×tbabs×(bbody×polconst+trcpow×polconst)									
$kT_{\text{BB1}}$ keV	norm <sub>BB1</sub> × 10 <sup>-3</sup>	PD <sub>BB1</sub>	PA <sub>BB1</sub> deg	Γ	norm <sub>PL</sub> × 10 <sup>-1</sup>	$E_{\text{trc}}$ keV	PD <sub>PL</sub>	PA <sub>PL</sub> deg	χ <sup>2</sup>
0.448 <sup>+0.001</sup> <sub>-0.002</sub>	2.07 <sup>+0.05</sup> <sub>-0.01</sub>	0.168 <sup>+0.008</sup> <sub>-0.008</sub>	48.2 <sup>+1.4</sup> <sub>-1.4</sub>	2.67 <sup>+0.04</sup> <sub>-0.07</sub>	0.27 <sup>+0.02</sup> <sub>-0.02</sub>	3.38 <sup>+0.07</sup> <sub>-0.02</sub>	0.23 <sup>+0.04</sup> <sub>-0.04</sub>	-43.9 <sup>+5.4</sup> <sub>-5.4</sub>	1425.6